

BubbleONet: A Physics-Informed Neural Operator for High-Frequency Bubble Dynamics

Yunhao Zhang¹, Lin Cheng², Aswin Gnanaskandan^{1,*}, Ameya D. Jagtap^{3,*}

¹ *Department of Mechanical and Materials Engineering, Worcester Polytechnic Institute, 100 Institute Road, Worcester, 01609, MA, USA.*

² *Department of Mechanical Engineering, University of Maryland, 841 Campus Dr, College Park, 20742, MD, USA.*

³ *Department of Aerospace Engineering, Worcester Polytechnic Institute, 100 Institute Road, Worcester, 01609, MA, USA.*

Abstract

This paper introduces BubbleONet, an operator learning model designed to map pressure profiles from an input function space to corresponding bubble radius responses. BubbleONet is built upon the Physics-Informed Deep Operator Network (PI-DeepONet) framework, leveraging DeepONet’s powerful universal approximation capabilities for operator learning alongside the robust physical fidelity provided by physics-informed neural networks. To mitigate the inherent spectral bias in deep learning, BubbleONet integrates the Rowdy adaptive activation function, enabling improved representation of high-frequency features. The model is evaluated across various scenarios, including: (1) Rayleigh–Plesset equation based bubble dynamics with a single initial radius, (2) Keller–Miksis equation based bubble dynamics with a single initial radius, and (3) Keller–Miksis equation based bubble dynamics with multiple initial radii. Moreover, the performance of single-step versus two-step training techniques for BubbleONet is investigated. The results demonstrate that BubbleONet serves as a promising surrogate model for simulating bubble dynamics, offering a computationally efficient alternative to traditional numerical solvers.

Keywords: Physics Informed Neural Network, Bubble dynamics, Operator learning, Rayleigh–Plesset equation, Keller–Miksis equation

1. Introduction

Microscopic gas bubbles are integral to a wide range of scientific and engineering applications, including medical techniques like ultrasound-mediated drug delivery [1], thermal ablation [2], and industrial operations such as cavitation-based jet cleaning [3]. On the other hand, cavitating bubbles also have harmful effects such as erosion and noise generation [4], thus making an in-depth understanding of bubbles imperative to both harnessing their benefits and mitigating their harmful effects. The dynamic behavior of these oscillating bubbles is traditionally described by models such as Rayleigh–Plesset (R-P) equation [5, 6, 7], Keller–Miksis (K-M) equation [8], Keller–Herring equation [9], and Gilmore equation [10]. These models offer essential theoretical understanding of single-bubble dynamics. However, their extension to systems involving multiple interacting bubbles introduces significant computational challenges. The resulting complexity and high computational cost often hinder their feasibility in real-time analysis and large-scale simulations.

*Corresponding Authors: agnanaskandan@wpi.edu (Aswin Gnanaskandan), ajagtap@wpi.edu (Ameya D. Jagtap)

The rapid advancement of machine learning has opened new avenues for developing surrogate models that can augment or even replace traditional numerical solvers for complex physical systems; a research direction now widely recognized as scientific machine learning (SciML). Among emerging approaches, neural operator-based frameworks have garnered significant attention for their ability to learn mappings between infinite-dimensional function spaces. A leading example is the Deep Operator Network (DeepONet), introduced by Lu *et al.* [11], which is theoretically grounded in the universal approximation theorem for operators. The DeepONet architecture comprises of two subnetworks: a branch network that encodes the input function and a trunk network that represents the output domain. Their outputs are combined to predict the target function, enabling the model to learn nonlinear operator mappings effectively. Since its introduction, DeepONet has been widely adopted and extended across a range of scientific disciplines. For instance, Mao *et al.* [12] developed DeepM&Mnet to model chemical dissociation reactions, while Jin *et al.* [13] proposed MIONet for multi-input operator regression, applying it to coupled diffusion–reaction systems. Peyvan *et al.* [14] designed a two-step training methodology to enhance DeepONet’s performance on the Riemann problem, and Goswami *et al.* [15] introduced a Partition-of-Unity (PoU) DeepONet framework for learning operators in chemical kinetics and turbulent flows. Additionally, Osorio *et al.* [16] explored the use of DeepONet for forecasting dynamics in solar-thermal energy systems. Collectively, these developments underscore DeepONet’s potential as a general-purpose tool for solving physics-informed problems through operator learning over functional spaces.

Another prominent framework for solving physics-governed problems is the Physics-Informed Neural Network (PINN). The central idea behind PINNs is the incorporation of physical laws, typically expressed as partial differential equations, directly into the loss function of neural networks, thereby guiding the training process through the underlying governing equations [17]. Since their introduction by Raissi *et al.* [17], PINNs have been widely adopted in diverse scientific and engineering domains. By embedding physical constraints, PINNs are capable of generating highly accurate solutions while substantially reducing dependence on large labeled datasets, distinguishing them from purely data-driven models [17, 18]. To address limitations related to scalability and computational efficiency, several enhanced variants of the original PINNs framework have been developed. Notable examples include Conservative PINNs [19] and eXtended PINNs (XPINNs) [20], which leverage conservation principles and domain decomposition strategies to improve performance; see also [21, 22] for unified temporal decomposition and adaptive domain decomposition, respectively. These innovations have enabled the application of PINNs to increasingly complex and high-dimensional problems. For example, Shukla *et al.* [23] employed PINNs for the identification of material properties, while Jagtap *et al.* [24] addressed inverse nonlinear water wave problems. Abbasi *et al.* [25] developed PINN-based workflows for porous media; see also their survey on PINNs applied to shock waves [26]. Zhu *et al.* [27] constructed a surrogate PINN model to simulate melt pool dynamics in metal additive manufacturing, and Mao *et al.* [28] applied PINNs to the analysis of high-speed compressible fluid flows; see also Jagtap *et al.* [29] for solving inverse problems in high-speed flows. Cheng *et al.* [30] integrated PINNs into a representative volume element (RVE) framework to capture structure–property relationships in heterogeneous materials. Furthermore, Zhu *et al.* [31] employed PINNs for surrogate modeling aimed at uncertainty quantification. PINNs have also been employed for the solution of high-dimensional partial differential equations [32, 33]. The foundational mathematical theory underlying PINNs and their extended variants (XPINNs) has been developed by several authors [34, 35, 36]. A comprehensive survey of the approximation theory for physics-informed machine learning is provided by Mhaskar *et al.* [37].

The application of machine learning to bubble dynamics remains relatively underexplored. Lin *et al.* [38, 39] employed DeepONet to investigate multi-scale bubble behavior. However, their study

addresses only a limited subset of the broader problem and exhibits several notable limitations. First, the pressure profiles in their simulations are generated using Gaussian random fields, which do not accurately reflect the sinusoidal nature of pressure variations encountered in various practical applications. Second, their dataset is constrained to low amplitude pressure fluctuations on the order of 10^3 Pa, whereas realistic scenarios often involve amplitudes up to 10^6 Pa. Additionally, a critical limitation lies in their exclusive focus on low-frequency excitations. Bubble dynamics can vary significantly under different frequency regimes, and the absence of high-frequency data impairs the model’s generalizability. These limitations emphasize the necessity for a more comprehensive machine learning framework for modeling bubble dynamics.

The objective of this study is to develop a Physics-Informed Deep Operator Network (PI-DeepONet). The proposed model, named *BubbleONet*, is designed to provide a robust and generalizable computational framework for the simulation of complex bubble dynamics. Wang [40] demonstrated the effectiveness of PI-DeepONet in solving a variety of partial differential equations, further reinforcing its potential for modeling intricate bubble dynamics. Goswami *et al.* [41] applied the PI-DeepONet to predict crack elongation in quasi-brittle materials. Lu *et al.* [42] employed PI-DeepONet to solve fluid dynamics problems, including diffusion and advection equations.

The remainder of this paper is organized as follows. Section 2 discusses the limitations of the original DeepONet architecture in learning R-P equation-based bubble dynamics. Section 3 presents the governing equations examined in this study, the R-P equation and K-M equation. Section 4 introduces the proposed solutions to the challenges faced in previous studies, including the incorporation of adaptive activation functions and physics-based constraints. Section 5 presents the simulation results, ranging from a single-step initial radius based on R-P and K-M equations to multiple initial radius cases based on the K-M equation. Further, a comparison between the single-step training technique and the two-step training technique is also presented. To this end, Section 6 concludes the study with a summary of findings, limitations, and future directions.

2. Evaluating the Constraints of the Original DeepONet Approach to Bubble Dynamics

Lin *et al.* [38, 39] effectively employed this architecture to investigate bubble dynamics governed by the Rayleigh–Plesset equation. In their framework, the branch network takes the pressure variation ΔP as input, where the imposed pressure is defined as $P_\infty = P_0 + \Delta P$, consistent with the assumption of small amplitude fluctuations. Here, P_0 represents the initial pressure. The trunk network receives time as its input. Both the branch and trunk networks are implemented as standard feedforward neural networks (FFNNs), and their outputs are combined through a dot product to generate the final prediction.

Table 1: Design of Experiments for generating training and validation data

Parameters	Range	Intervals
Initial radius, R_0 (μm)	50	1
Pressure amplitude, amp (Pa)	$[1, 10] \times 10^5$	10
Pressure frequency, f (kHz)	[200, 2000]	300

To evaluate the generalization capability of the model, we initially employed the original DeepONet architecture to simulate bubble dynamics. The training data were generated using the open-source code APECSS [43], which numerically solves the Rayleigh–Plesset equation. To address the limitations discussed earlier, a total of 3,000 datasets driven by sinusoidal pressure profiles were generated following the design of experiments (DoE) outlined in Table 1, with 2,400

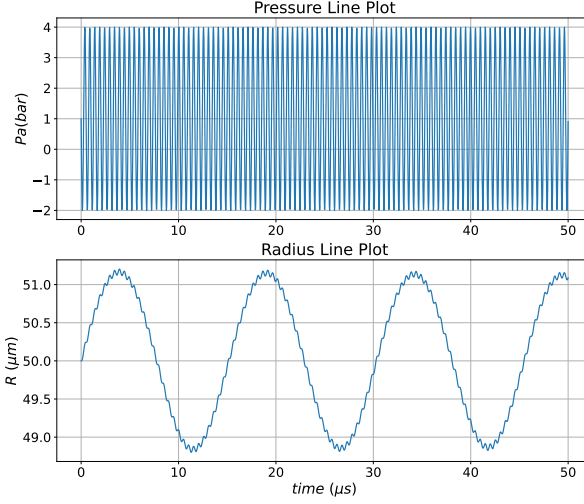


Figure 1: Sample bubble dynamics simulation obtained from APECSS for a bubble with $R_0 = 50\mu m$, $f = 1970kHz$, $amp = 3 \times 10^5 Pa$, $t = 50\mu s$. Top: pressure profile. Bottom: Radius evolution

datasets used for training and 600 for validation. An example from the dataset is shown in Figure. 1, corresponding to a bubble with an initial radius of $R_0 = 50\mu m$, subjected to an acoustic pressure field with a frequency of $f = 1337.4kHz$ and an amplitude of $6 \times 10^5 Pa$ over a time span of $50\mu s$.

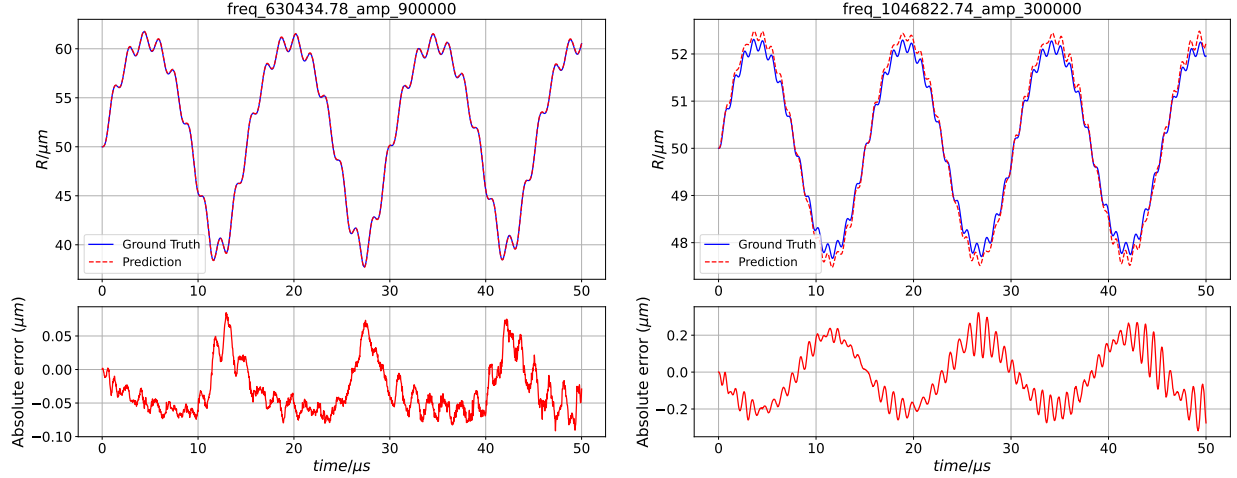


Figure 2: Validation results from R-P equation using the original DeepONet after 500,000 epochs. (a)Bubble dynamics driven by pressure with frequency of 630.4 kHz and amplitude of $9 \times 10^5 Pa$, representing low frequency case. (B)Bubble dynamics driven by pressure with frequency of 1046.8 kHz and amplitude of $3 \times 10^5 Pa$, representing high frequency case

Figure. 2 presents the predictions generated by the original DeepONet architecture after training. Two representative cases of pressure-driven bubble dynamics are shown, both with an initial radius of $R_0 = 50\mu m$. Case 1 corresponds to a pressure signal with a frequency of 630.43 kHz and an amplitude of $9 \times 10^5 Pa$, while Case 2 involves a relatively higher frequency of 1046.82 kHz and a lower amplitude of $3 \times 10^5 Pa$. To optimize model performance, we explored multiple configurations of the branch and trunk networks, varying the depth from 3 to 8 layers and the width from 128 to 512 neurons. The results displayed in Figure 2 correspond to the best-performing configuration, 8 layers with 512 neurons per layer, trained for 500,000 epochs, which yielded the lowest training and validation losses. Figure 2a illustrates the online prediction for Case 1, where the model output

closely aligns with the ground truth with the low absolute error confirming the model’s ability to capture low-frequency bubble dynamics with high accuracy, where absolute error is defined as online prediction minus ground truth. In contrast, Figure 2b shows the prediction for Case 2, where the model captures the overall trend but fails to resolve the finer details of the high-frequency oscillations. This behavior is further exacerbated in cases involving ultra-high frequencies (e.g., 1900 kHz and 2000 kHz). These observations underscore the spectral bias inherent to the original DeepONet architecture. More details on the preliminary study on the original model can be found in [44].

3. Governing Equations

The physics of bubble dynamics is well characterized by mathematical models. We utilize two different equations: the Rayleigh–Plesset equation, a fundamental ordinary differential equation (ODE) that describes the idealized radial motion of a spherical bubble in an incompressible liquid [45, 6, 7], and the Keller–Miksis equation, a more comprehensive model that accounts for liquid compressibility and acoustic effects to more accurately capture bubble behavior [8].

3.1. Rayleigh-Plesset equation

Assuming a spherical bubble, the governing equation can be written as:

$$R\ddot{R} + \frac{3}{2}\dot{R}^2 = \frac{1}{\rho} \left(P_G - P_\infty - 4\mu\frac{\dot{R}}{R} - \frac{2S}{R} \right), \quad (1)$$

where R denotes the bubble radius as a function of time t , evolving under the influence of the far-field pressure P_∞ . Thus, \dot{R} and \ddot{R} represent the first and second order derivative of R accordingly. Here, S represents the surface tension coefficient, μ is the dynamic viscosity of the liquid, and ρ is the liquid density. P_G is the internal gas pressure, modeled as:

$$P_G = P_{G0} \left(\frac{R_0}{R} \right)^{3k}. \quad (2)$$

Here, P_{G0} corresponds to the initial internal gas pressure $P_G(t = 0)$. The exponent $k = 1.4$ is the polytropic coefficient, reflecting the adiabatic behavior of the gas. To ensure consistency between the training process and the governing physical laws, we employ the non-dimensional form of the R–P equation for normalization. This avoids potential numerical errors during mathematical operations. The derivation of the non-dimensional form and the numerical solution methodology using Runge-Kutta method can be found in Appendix A.

3.2. Keller-Miksis equation

With the same assumptions used for the R–P equation, except for the incompressibility of the liquid medium, the K–M equation can be expressed as

$$\left(1 - \frac{\dot{R}}{c} \right) R\ddot{R} + \frac{3}{2} \left(1 - \frac{\dot{R}}{3c} \right) \dot{R}^2 = \left(1 + \frac{\dot{R}}{c} \right) \frac{P_L - P_\infty}{\rho} + R \frac{\dot{P}_L - \dot{P}_\infty}{\rho c}, \quad (3)$$

where

$$P_L = P_G - 4\mu\frac{\dot{R}}{R} - \frac{2S}{R},$$

$$\dot{P}_L = \dot{P}_G + 4\mu \left(\frac{\dot{R}^2}{R^2} - \frac{\ddot{R}}{R} \right),$$

Here, c denotes the speed of sound in the liquid, while all other variables are the same as in the R-P equation. The derivation of the non-dimensional form and the numerical solution methodology using Runge Kutta method can be found in Appendix B.

4. Methodology: A Physics-Informed Operator Learning Architecture for Simulating Bubble Dynamics

In this section, we present the architecture of BubbleONet, illustrated in Figure 3. The model comprises of two primary components: the operator layer and the operation layer. The operator layer exploits the operator approximation capabilities of the DeepONet and integrates an adaptive activation function inspired by the deep Kronecker neural network (KNN) [46]. Then, the operation layer embeds physical constraints into the learning framework to help prevent nonphysical predictions and ensure consistency with the underlying physics.

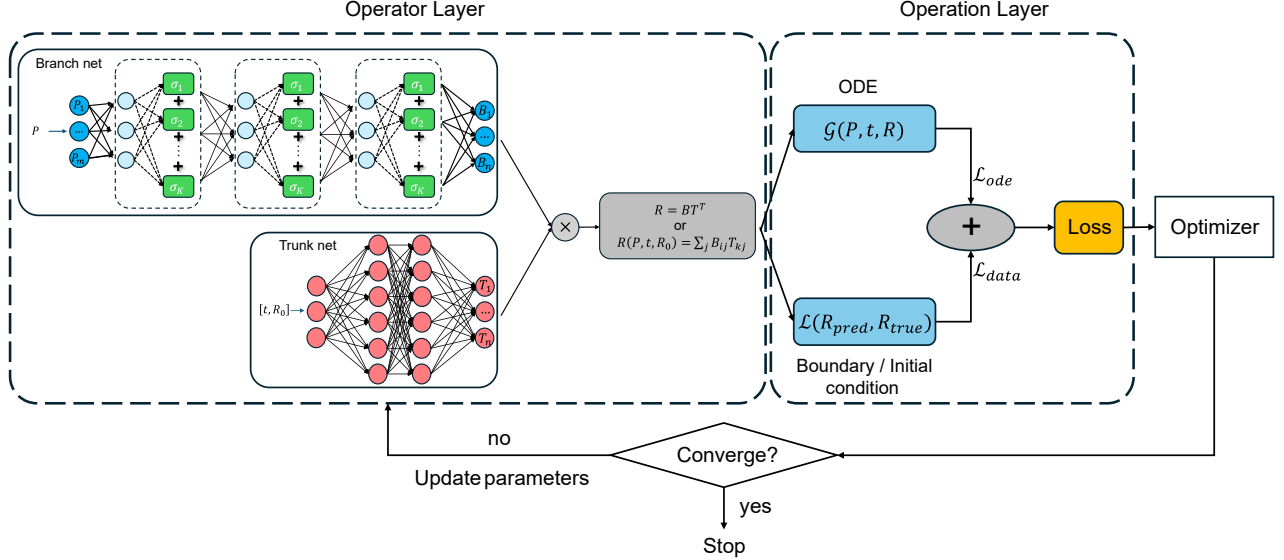


Figure 3: The architecture of BubbleONet consists of an operator layer and an operation layer. The operator layer is built on a Deep Operator Network, with a Kronecker neural network - based branch net that takes the full pressure profile as input, and a feedforward trunk net that takes time and initial radius as input. The operation layer post-processes the output to enforce physical constraints. The loss combines data and ODE components, and the optimizer updates the network parameters iteratively until convergence.

4.1. Branch net with adaptive activation function to address spectral bias

Deep learning models exhibit a well-documented phenomenon known as spectral bias, characterized by the tendency to preferentially learn simpler (low-frequency) functions over more complex (high-frequency) ones. This bias emerges not only from the training dynamics but also from the intrinsic structure and parameterization of neural networks [47, 48]. To address spectral bias, adaptive activation functions have proven effective by introducing bounded yet highly non-monotonic fluctuations into network outputs, thereby reducing saturation across layers and preserving sensitivity to high-frequency features [46]. Similar approaches are employed in the noise activation function introduced by Gulcehre [49] and the probabilistic activation function proposed

by Shridhar [50]. Furthermore, adaptive activation functions enhance model performance [51] and promote smoother convergence in various deep learning frameworks, including physics-informed neural networks [52, 53]. See the comprehensive survey of activation functions by Jagtap and Karniadakis [54].

Jagtap et al.[46] introduced the Rowdy activation function, augmenting standard activation functions with sinusoidal components to effectively capture high-frequency solutions to the Helmholtz equation. This formulation was subsequently extended by incorporating a phase adjustment term, further improving the model’s capability to solve the Riemann problem[14]. Motivated by these advances, we integrate the Rowdy activation function into our BubbleONet architecture to alleviate spectral bias and enhance the network’s ability to represent high-frequency features. We begin by considering a feed-forward neural network (FFNN), expressed mathematically as follows:

$$\mathbf{y}^{(l)} = \sigma^l (\mathbf{W}^{(l)} \mathbf{y}^{(l-1)} + \mathbf{b}^{(l)}) , \quad (4)$$

where $\mathbf{y}^{(l)}$ represents the output of layer l , $\mathbf{W}^{(l)}$ is the weight matrix of layer l , $\mathbf{y}^{(l-1)}$ is the input from the previous layer $l - 1$, $\mathbf{b}^{(l)}$ is the bias vector of layer l , $\sigma(\cdot)$ is the activation function. Assuming a block activation function $\vec{\sigma}$ represented as:

$$\vec{\sigma}(\mathbf{h}) = \begin{bmatrix} \sigma_1(h) \\ \vdots \\ \sigma_K(h) \end{bmatrix} , \quad (5)$$

In our case, σ_1 is the ReLU activation function and K is a positive integer of 5. The remaining functions $\{\sigma_k\}_{k=2}^K$:

$$\sigma(x) = n \sin((k-1)nx) , \quad \forall 2 \leq k \leq K, \quad (6)$$

Thus, using h denoting the linear operation of $\mathbf{h}^{(l)} = \mathbf{W}^{(l)} \mathbf{y}^{(l-1)} + \mathbf{b}^{(l)}$, Eq 4 is written as:

$$\begin{aligned} \mathbf{y}^{(l)} = & \text{ReLU}(n * a_0 * \mathbf{h}^{(l)}) \\ & + \sum_{i=1}^{K-1} n * a_i * \sin(n * F_i * \mathbf{h}^{(l)} + c_i) \end{aligned} \quad (7)$$

where n is the scaling factor set to 10 to scale the amplitude of the introduced noise, and a_i and c_i denote the amplitude and phase terms of the sinusoidal components. These terms are treated as learnable parameters within the neural network. a_i and c_i are initialized to 0, except for a_0 , which is set to 0.1 to ensure that the network initially behaves similarly to a standard ReLU activation function. The Rowdy activation function is integrated into the branch network, as this component is responsible for constructing the latent representation of the input frequency-related function. Accordingly, the FFNN is replaced by a Kronecker Neural Network. Incorporating the Rowdy activation is crucial for introducing additional learnable parameters on frequencies and phases, thereby enhancing the model’s ability to capture complex bubble dynamics.

As discussed in the previous section, due to the large magnitude of the pressure amplitude, using ΔP as the input to the branch network is inadequate for representing the global input function space. Instead, BubbleONet directly uses the pressure profile as the input to the branch network, with the output of latent variable B that includes the extracted features. As for the trunk network, it primarily encodes the time domain and the initial radius into a latent representation T in a higher-dimensional space. A standard FFNN is sufficient to extract the necessary features in this context. The final output $R(P, t, R_0)$ is computed through a linear operation on the latent variable:

$$R(P, t, R_0) = BT^\top , \quad (8)$$

where $B \in \mathbb{R}^{m \times d}$ and $T \in \mathbb{R}^{n \times d}$, specifically, n is the length of time, m is batch size, and d is the length of latent variable. To ensure the positivity of the predicted radius, a *SmoothReLU* (*softplus*) activation is applied to R , thus preventing nonphysical negative radius predictions.

4.2. Loss Function

With the inclusion of physical constraints, the loss function consists of two components: a *data loss* ($\mathcal{L}_{\text{data}}$) term from the neural network predictions and an *ODE loss* (\mathcal{L}_{ode}) term derived from the governing equation. Let \mathcal{L} denote the mean squared error (MSE) loss function. The total loss is defined as:

$$\begin{aligned} \text{Loss} &= w_{\text{data}} \mathcal{L}_{\text{data}} + w_{\text{ode}} \mathcal{L}_{\text{ode}} \\ &= w_{\text{data}} \times \frac{1}{N_d} \sum_{i=1}^{N_d} \|R_i - \bar{R}_i\|_2^2 + w_{\text{ode}} \times \frac{1}{N_c} \sum_{i=1}^{N_c} \|\mathcal{G}(R_i)\|_2^2, \end{aligned} \quad (9)$$

where $\mathcal{L}_{\text{data}}$ denotes the discrepancy between the predicted radius profile R and the ground truth \bar{R} , with R_i representing the i th sample in the dataset of size N_d and N_c represents the number of collocation points. The symbol $\|\cdot\|_2$ indicates the L2 norm. The ODE loss \mathcal{L}_{ode} represents the discrepancy in the governing dynamics, where $\mathcal{G}(\cdot)$ is the Runge–Kutta-based numerical operator for the governing ODE with discrete scheme form as:

$$\mathcal{G}(R_N) := y_{N+1} - (y_N + dt \sum_{j=1}^s b_j k_j), \quad (10)$$

where dt is the time step size, s is the number of Runge–Kutta stages, and b_j is the stage weights of stage j . The subscript N refers to the current time step in matrix form. The state matrix y is defined as:

$$y = \begin{bmatrix} R \\ \dot{R} \end{bmatrix} \quad (11)$$

The computation of the intermediate stages k_j , as well as the coefficients b_j , follows the RK5(4)7M formulation and can be found in [55], where stage number is 7 with 5th-order accuracy. The weights w_{data} and w_{ode} are hyperparameters that balance the contributions of the data-driven loss and the physics-informed residual loss.

5. Results and Discussion

In this section, three simulation cases are discussed. The first case involves bubbles solved using R–P equation with a single initial radius of $R_0 = 50 \mu\text{m}$, representing the simplest scenario. The second case considers bubbles solved using K–M equation with the same initial radius, $R_0 = 50 \mu\text{m}$, introducing liquid compressibility effects compared to the R–P model. The third case extends the K–M model to multiple initial radii, aiming to evaluate the model’s capability in capturing bubble dynamics in higher-dimensional parameter spaces. Model training was conducted on an NVIDIA GeForce RTX 3070 GPU with 8 GB of memory, paired with an Intel Core i7-12700 CPU and 25.4 GB of system RAM. The Adam optimizer was chose for progressing the training. The hyperparameters for each of the above cases are listed in Table 2

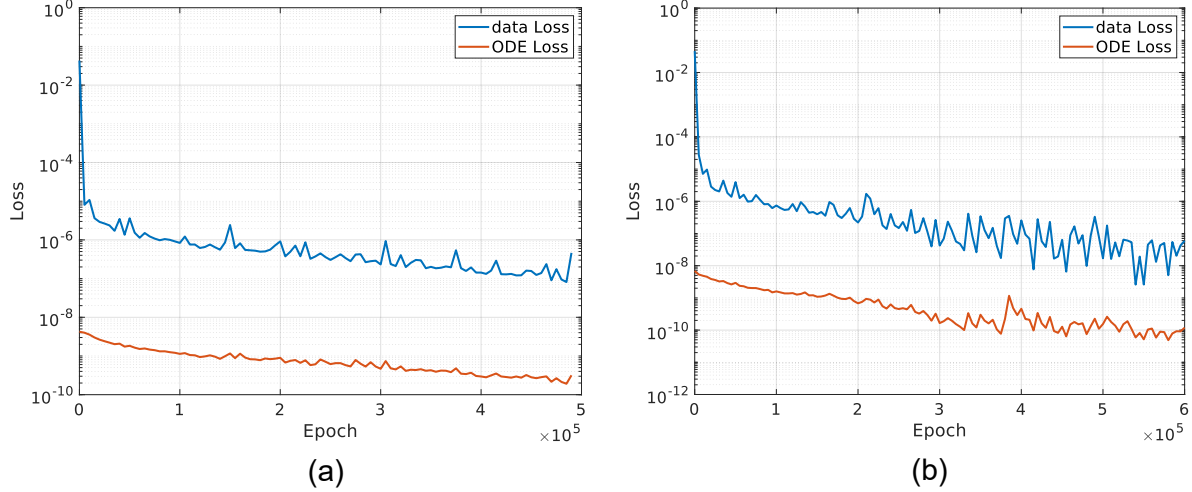


Figure 4: Convergence history showing both data loss and residual loss from ODE for bubbles simulated using (a) R-P equation (b) K-M equation

Table 2: Hyperparameters used in each subsection

Subsection	Learning rate	Batch size	Architecture
Section 5.1	0.0005	200	Branch net: [2000, 512, 512, 512, 512, 512, 512, 512] Trunk net: [1, 512, 512, 512, 512, 512, 512, 512]
Section 5.2	0.0005	200	Branch net: [2000, 512, 512, 512, 512, 512, 512, 512] Trunk net: [1, 512, 512, 512, 512, 512, 512, 512]
Section 5.3	0.0001	200	Branch net: [2000, 512, 512, 512, 512, 512, 512, 512] Trunk net: [1, 512, 512, 512, 512, 512, 512, 512]
Section 5.4	0.0001	25	Branch net: [2000, 512, 512, 512, 512, 512, 512, 512] Trunk net: [2, 512, 512, 512, 512, 512, 512, 512]

5.1. Bubble Dynamics Governed by the R-P Equation with Single Initial Radius

The Rayleigh–Plesset equation is a nonlinear ODE that describes the dynamics of a spherical bubble in an infinite, incompressible, and viscous liquid. It serves as a fundamental model in bubble dynamics and cavitation physics [5, 6, 7]. In this section, we evaluate the model’s learning capability and performance on this simplest scenario.

5.1.1. Performance

The model is trained using data simulated according to the design of experiments described in Table 1. Out of 3000 datasets, 2400 are randomly selected for training and 600 for validation, with each simulation lasting $50 \mu\text{s}$ and cut into data shape of 2000. The model is trained for 500,000 epochs. As this case involves single-radius prediction, the initial condition is not explicitly enforced. Therefore, the loss function simplifies to:

$$\text{Loss} = \mathcal{L}_{\text{data}} + 100 * \mathcal{L}_{\text{ode}} \quad (12)$$

The weights of 1 and 100 are chosen based on the initial loss at epoch 0 to ensure that each term is reduced simultaneously. The training loss is shown in Figure 4(a), where the neural network loss

\mathcal{L}_{data} decreases rapidly at the beginning and gradually continues to decline as training progresses, while the governing equation loss \mathcal{L}_{ode} steadily decreases throughout.

A high-frequency validation case simulated with a frequency of 1900 kHz and an amplitude of 2×10^5 Pa is used to evaluate the model performance at different training epochs, as illustrated in Figure 5. This figure provides a clear visualization of how the model gradually learns the features during training. For each validation, three plots are presented: (1) a comparison between the ground truth and the online prediction, (2) the corresponding absolute error (ground truth minus prediction), and (3) response in the frequency domain obtained via Fast Fourier Transform (FFT). In bubble dynamics, two peaks are typically observed in the frequency domain: the first corresponds to the natural frequency, and the second arises from the driving frequency of the external pressure field P_∞ . Resonance occurs when these two frequencies coincide.

At epoch 100,000, the model successfully captures the natural frequency but struggles to learn the driving frequency, resulting in an absolute error within the range of $[-0.05, 0.05] \mu\text{m}$, which corresponds to approximately 0.01% of the initial radius ($50 \mu\text{m}$). At this stage, the second FFT peak is noticeably shifted from that of the ground truth, as indicated by the green circle. By epoch 300,000, the model begins to capture the driving frequency, and the absolute error near the start of the simulated time domain decreases. The second FFT peak also moves closer to the correct driving frequency. Finally, at epoch 500,000, the second FFT peak aligns well with the driving frequency, and the absolute error is further reduced to $[-0.02, 0.02] \mu\text{m}$. The predicted bubble radius closely matches the ground truth. This progressive learning is also reflected in the decreasing L_2 error, which drops from 4.18×10^{-5} to 2.16×10^{-5} .

For other cases, such as bubbles subjected to lower driving frequencies, the model finds it easier to learn the underlying dynamics. For instance, in the case of a bubble simulated with a frequency of 900 kHz and an amplitude of 3×10^5 Pa, the model produces satisfactory results after just 100,000 training epochs. The prediction error remains within the range $[-0.05, 0.05]$, and the corresponding MSE is 2.16×10^{-5} , as shown in Figure 6. Thus, we can conclude that the learning process of BubbleONet is from low to high in frequency domain, from left to right in the time domain.

5.2. Bubble Dynamics Governed by the K-M Equation with Single Initial Radius

Compared with the R-P equation, the K-M equation incorporates the compressibility of the liquid, providing a more accurate description of bubble dynamics, especially for high amplitude oscillations. This section focuses on the model's ability to learn such complex patterns.

5.2.1. Performance evaluation

A similar dataset is constructed based on the DoE shown in Table 1, with each dataset representing bubble dynamics simulated over $55 \mu\text{s}$ and comprising 2000 sampled data points. The loss function adopts the same formulation as in Eq. 12, and its convergence behavior is depicted in Figure. 4(b). The epoch is increased to 600,000, due to the complexity introduced by the compressibility of the liquid introduced in K-M equation. Both the neural network loss and the governing equation loss exhibit a learning trend comparable to that observed in the R-P case.

Three validation cases representing driving frequencies from different domains are shown in Figure. 7. The first case corresponds to a low frequency of 523 kHz and an amplitude of 9×10^5 Pa. In this case, noticeable discrepancies can be observed in the radius plot, with an absolute error on the order of 0.1 and an MSE of 1.59×10^{-3} . The second validation case is simulated at a frequency of 980 kHz and an amplitude of 3×10^5 Pa, representing a mid-range frequency in the design of experiments. The prediction aligns closely with the ground truth, with an absolute error

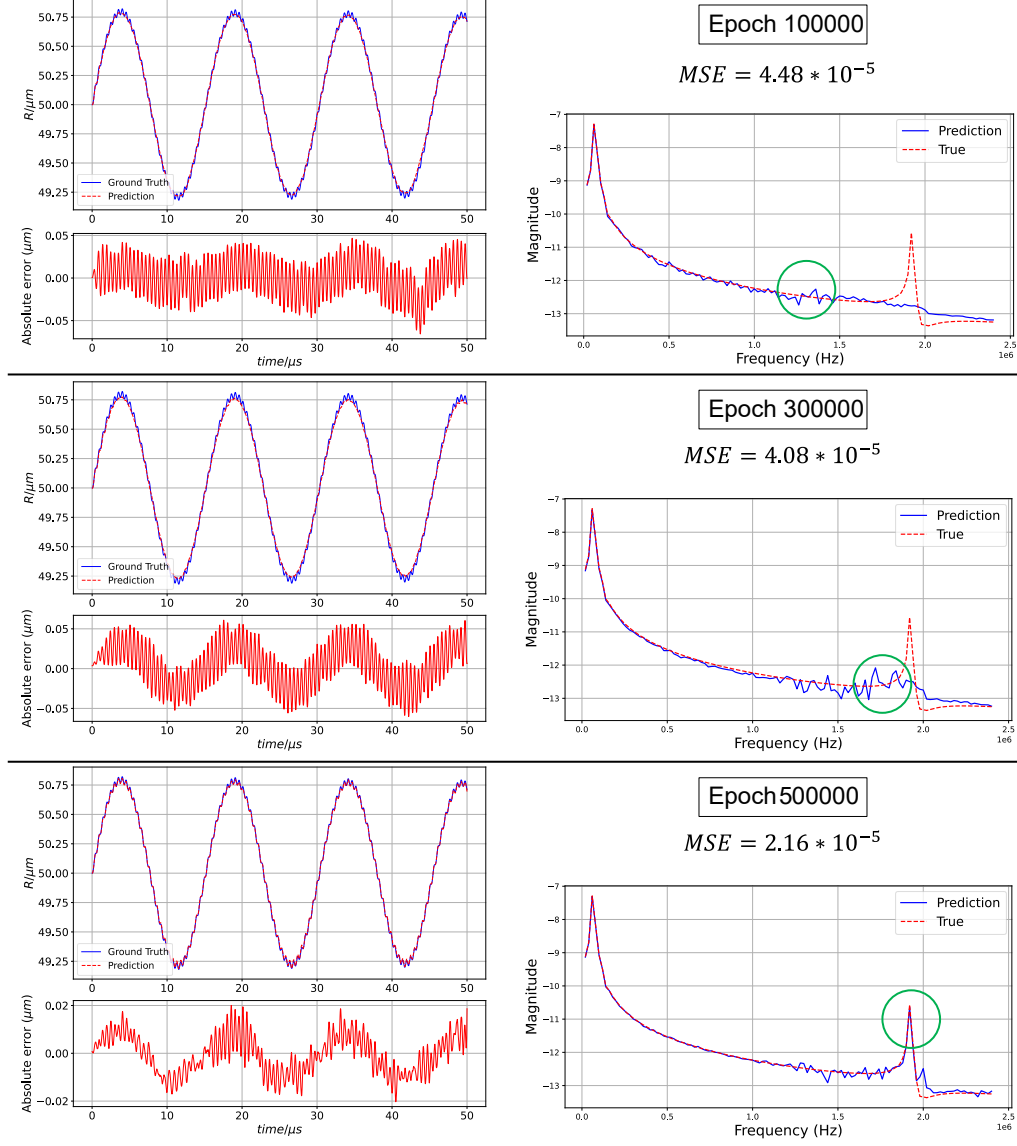


Figure 5: Validation of bubble dynamics simulated with a driving frequency of 1900 kHz and an amplitude of 2×10^5 Pa after 100,000, 300,000, 500,000 epochs and the corresponding data in frequency space.

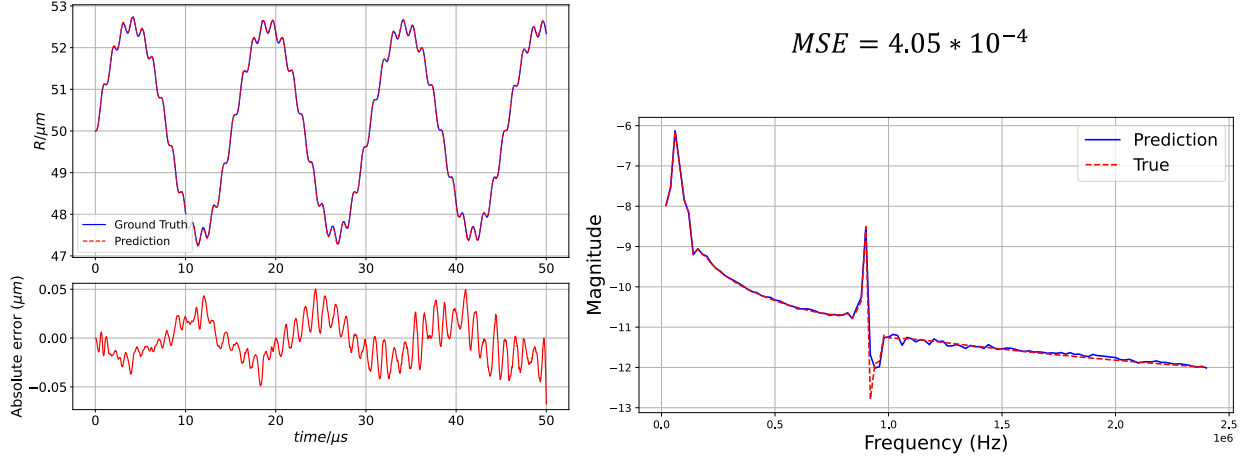


Figure 6: Validation of bubble dynamics simulated with a frequency of 900 kHz and an amplitude of 3×10^5 Pa after 100,000 epochs and the corresponding data in frequency space.

in the range of $[-0.025, 0.025]$ and an MSE of 3.60×10^{-4} . The final case corresponds to a high driving frequency of 1927 kHz and an amplitude of 8×10^5 Pa. The results demonstrate strong performance in this high-frequency regime, with an absolute error between $[-0.05, 0.05]$ and an MSE of 6.21×10^{-4} . Among the three cases, the model also consistently captures the damping effect due to liquid compressibility. Moreover, the driving frequency is accurately identified in the frequency domain across all scenarios.

5.2.2. Cross validation for generalization

Some validation cases, such as the bubble simulated with a frequency of 900 kHz and an amplitude of 9×10^5 Pa, exhibit noticeable discrepancies between the ground truth and the model prediction, as shown in Figure. 8. This may be due to the lack of similar features in the training data, leading to poor generalization in this particular case. To address this, a 5-fold cross-validation (CV) was conducted to enhance the model's robustness.

A comparison between the results of the directly trained model and the model trained with CV reveals a significant improvement. Specifically, the absolute error range decreases by an order of magnitude, from $[-0.6, 0.6]$ to approximately $[-0.06, 0.06]$. Notably, the frequency domain results indicate that even the directly trained model exhibits sufficient phase and frequency resolution to successfully capture the driving frequency, demonstrating the effectiveness of the rowdy activation function. However, the model fails to accurately predict the magnitude of the driving frequency component, i.e., it does not predict how strong the frequency response is, resulting in a mismatch between the predicted and true amplitudes. These findings suggest that the primary source of the discrepancy is likely due to data sparsity, rather than a fundamental inability to learn the frequency characteristics. As such, applying cross-validation helps alleviate this issue by improving the model's generalization performance in underrepresented regions of the parameter space.

5.2.3. Interpolation and extrapolation

To further investigate the model's generalization capability, both interpolation and extrapolation tests are conducted. As shown in Table 3, the data for this analysis are simulated using amplitudes of 5.5×10^5 Pa and 11×10^5 Pa, where the former lies within the range of the training data (interpolation), and the latter is outside the training range (extrapolation). The corresponding

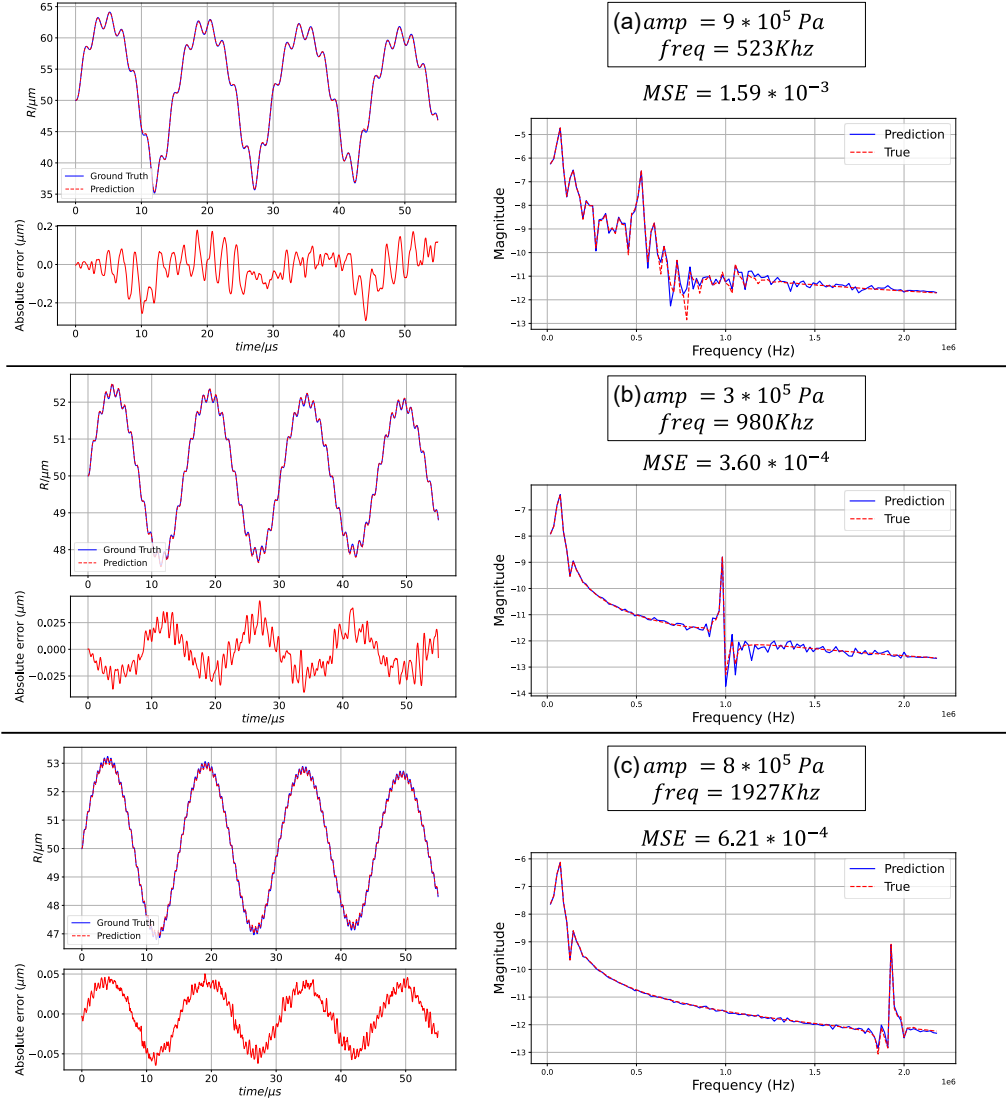


Figure 7: Validation of bubble dynamics (using K–M) simulated with: (a) a frequency of 523 kHz and an amplitude of 9×10^5 Pa, (b) a frequency of 980 kHz and an amplitude of 3×10^5 Pa, and (c) a frequency of 1927 kHz and an amplitude of 8×10^5 Pa, after 600,000 training epochs, along with the corresponding data in frequency space.

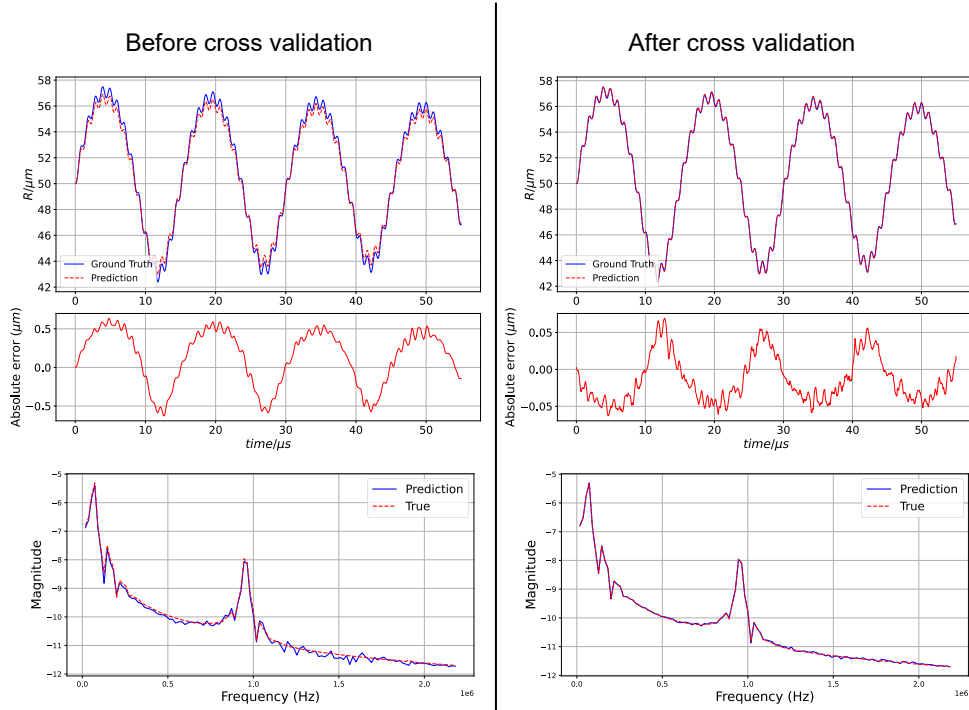


Figure 8: Effect of cross-validation on model generalization. The case of a bubble driven at 900 kHz and 9×10^5 Pa shows significant improvement in prediction accuracy after applying 5-fold cross-validation.

driving frequencies span from 600 kHz to 2500 kHz, with intervals of 100 kHz, resulting in a total of 40 datasets for this study.

Table 3: Design of experiments for interpolation and extrapolation

Parameters	Range	Numbers of Sampling
Pressure amplitude, amp (Pa)	$[5.5, 11] \times 10^5$	2
Pressure frequency, f (kHz)	[600, 2500]	20

The model used in this analysis is the optimized version obtained after applying cross-validation. Interpolation results at an amplitude of 5.5×10^5 Pa are presented in Figure. 9, with four representative frequencies: 600 kHz, 1000 kHz, 1300 kHz, and 2000 kHz.

- For the case of 600 kHz, the model performs well during the first half of the time series, but noticeable errors appear in the second half. The predicted radius exhibits reduced oscillation compared to the ground truth, which is also reflected in the frequency domain where the magnitude at the driving frequency is underestimated. This underperformance is generally observed in the range of 600 kHz to 800 kHz.
- When the frequency increases to the range of 900 kHz to 1200 kHz, the model predictions align well with the ground truth in both the time and frequency domains. For example, the case at 1000 kHz achieves an absolute error within the range of $[-0.02, 0.02]$.
- Prediction quality degrades again for frequencies between 1300 kHz and 1500 kHz. The case at 1300 kHz shows clear discrepancies in both the time domain and the spectral magnitude at the driving frequency.

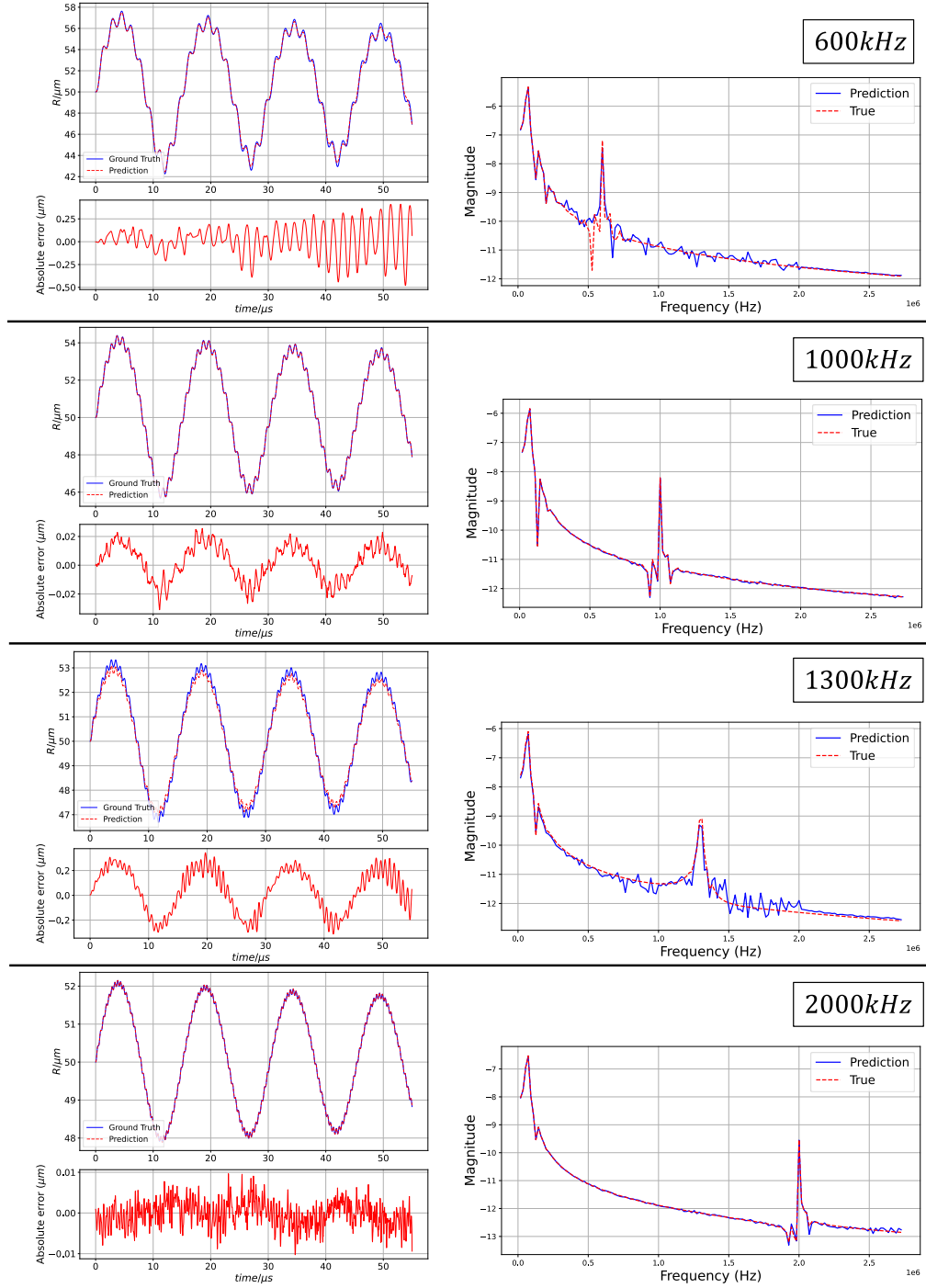


Figure 9: Time-domain and frequency-domain of interpolation results for bubbles simulated at 600 kHz, 1000 kHz, 1300 kHz, and 2000 kHz, with a fixed amplitude of 5.5×10^5 Pa.

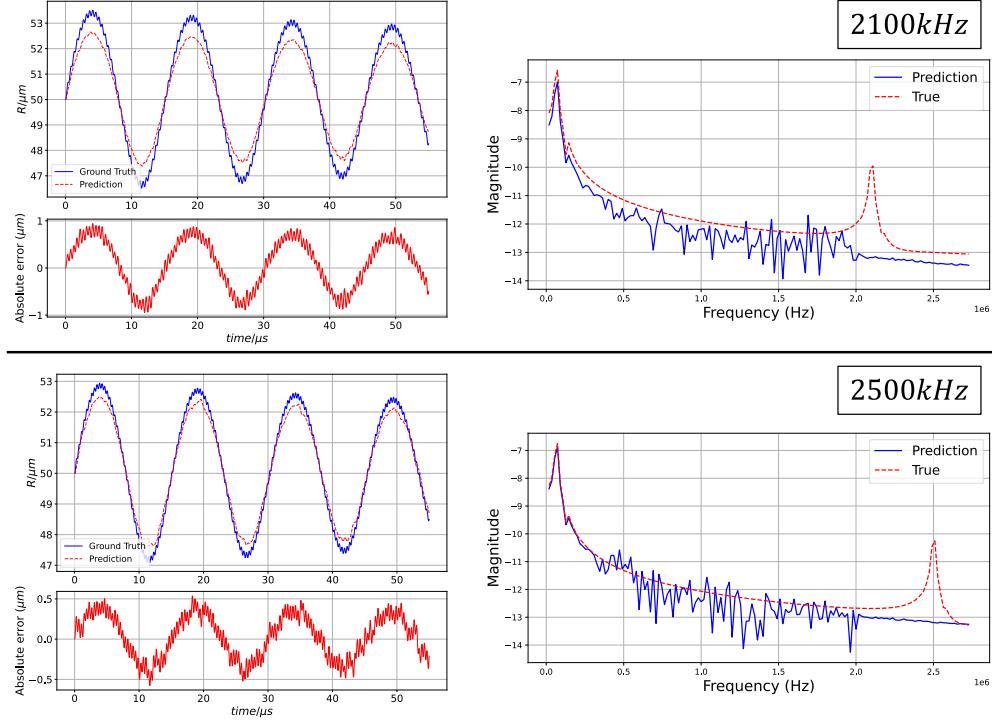


Figure 10: Time-domain and frequency-domain of extrapolation results for bubbles driven at 2100 kHz and 2500 kHz, with a fixed amplitude of 5.5×10^5 Pa.

- However, when the frequency increases further to the range of 1600 kHz to 2000 kHz, the model's performance improves significantly. For instance, the case at 2000 kHz demonstrates excellent agreement with the ground truth, with an absolute error confined within $(-0.01, 0.01)$.

Such periodical learning feature is likely due to sinusoidal function introduced in Rowdy activation function.

Two extrapolation cases at an amplitude of 5.5×10^5 Pa are presented in Figure. 10, corresponding to driving frequencies of 2100 kHz and 2500 kHz. Since these cases fall outside the function space used for operator learning, it is anticipated that the model may struggle to generalize. Indeed, both cases fail to accurately capture the driving frequency in the frequency domain. Nevertheless, a recurring learning pattern remains observable. In particular, the case at 2500 kHz exhibits smaller errors in the time domain and reduced discrepancies in the frequency spectrum. The corresponding MSE for each case are shown in Figure. 11 with blue color representing the interpolation and orange color representing the extrapolation, where a similar periodic pattern can be observed, further illustrating the model's frequency-dependent behavior.

For the extrapolation in terms of amplitude, two cases with an amplitude of 11×10^5 Pa at frequencies of 1000 kHz and 2000 kHz are shown in Figure. 12. In both cases, the absolute errors are reasonable ranging approximately within $[-1, 1]$ and $[-0.4, 0.4]$, with corresponding MSE of 0.56×10^{-3} and 4.10×10^{-3} , respectively. However, the driving frequencies are still accurately captured in the frequency domain. This suggests that the source of error is primarily due to the amplitude, as the model has not encountered similar features during training. These findings further confirm the sensitivity of the model to unseen amplitude ranges.

Another extrapolation study is conducted for a longer simulated time range, extending the

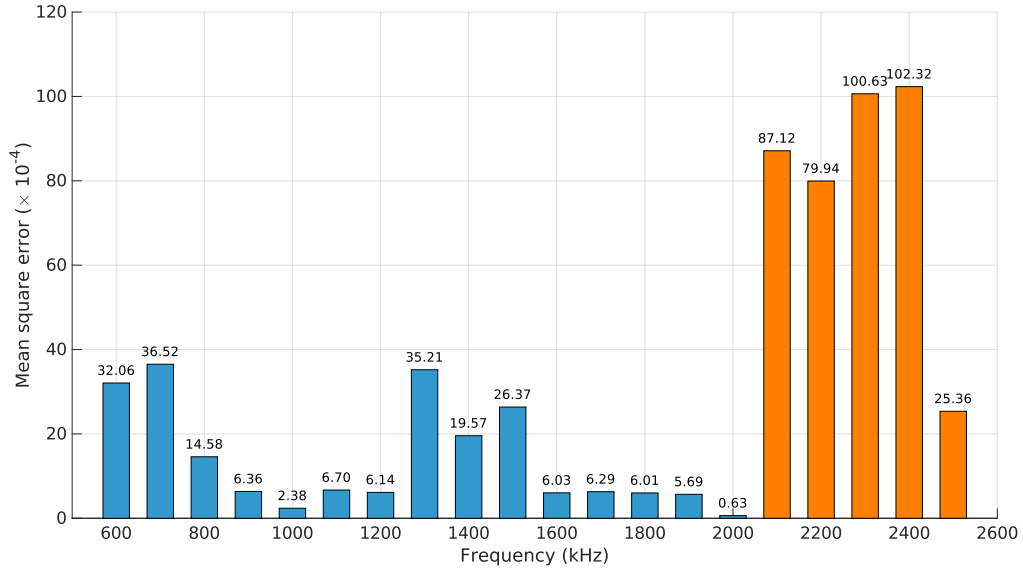


Figure 11: Mean square error across cases with frequencies ranging from 600 kHz to 2500 kHz, at a fixed amplitude of 5.5×10^5 Pa. Blue bars represent the frequencies learned by the model, while orange bars indicate frequencies outside the training domain.

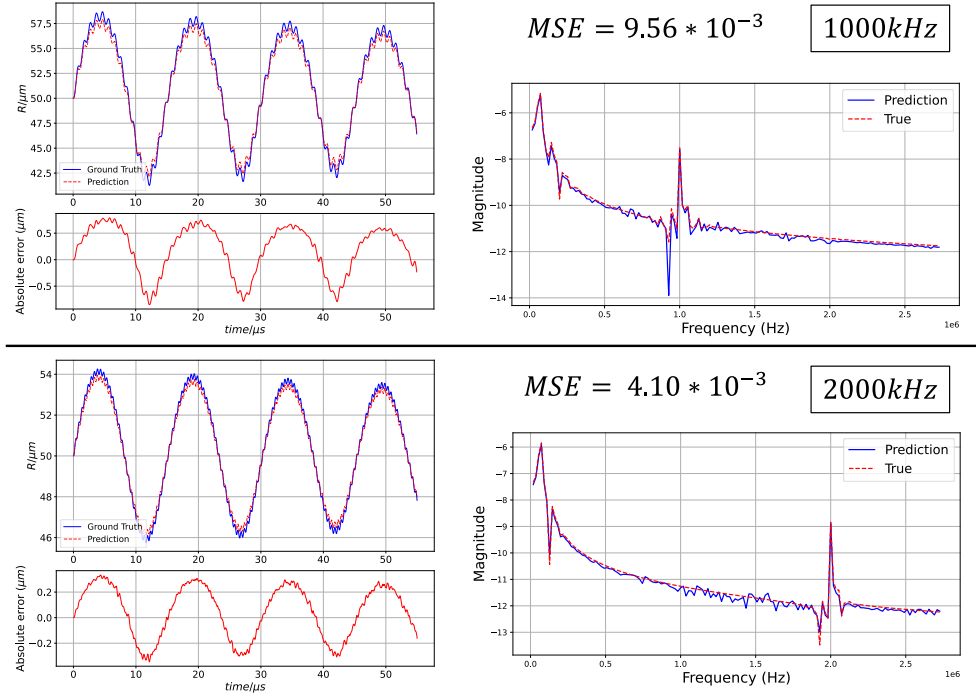


Figure 12: Time-domain and frequency-domain extrapolation results for bubbles driven at 1000 kHz and 2000 kHz, with a fixed amplitude of 11×10^5 Pa.

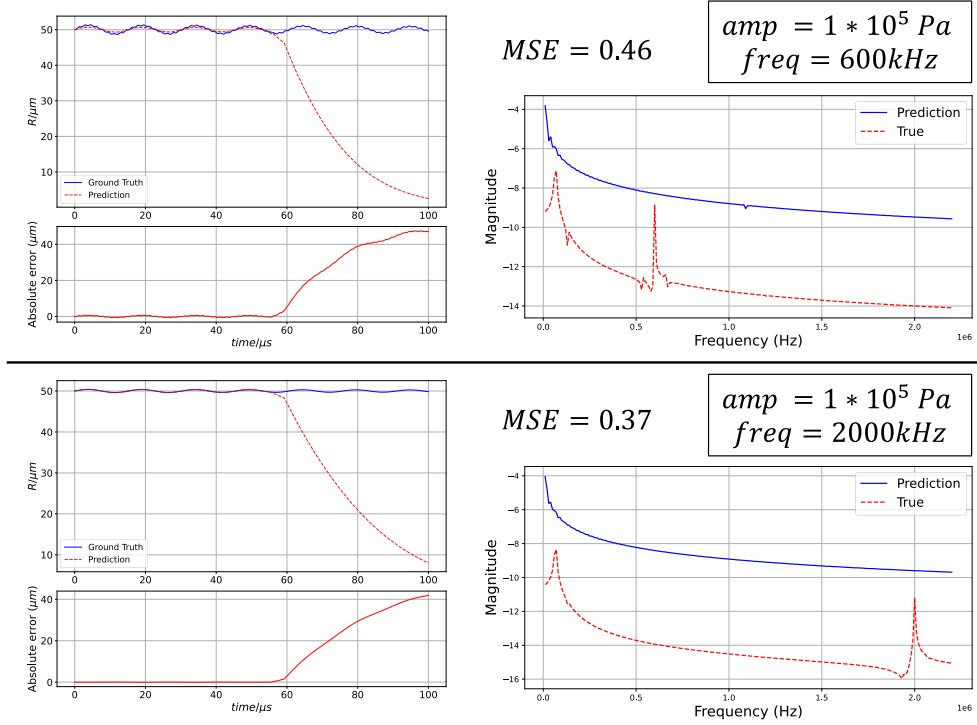


Figure 13: Time-domain and frequency-domain extrapolation results for bubble dynamics over $100\mu s$ driven at 600 kHz and 2000 kHz , with a fixed amplitude of $1 \times 10^5\text{ Pa}$.

original duration from $55\mu s$ to $100\mu s$. The results are shown in Figure. 13. In this scenario, the model fails to make accurate predictions, even within the time interval it was previously trained on, i.e., from 0 to $55\mu s$. Beyond this point, the predicted radius begins to shrink significantly, indicating that the model has entered a region outside of its learned function space. Further evidence of this failure is seen in the frequency domain, where the model is unable to capture either the natural frequency or the driving frequency, let alone their magnitudes. These results highlight the model’s limitation in generalizing to extended temporal domains.

5.3. Two-step training for K-M equation with single initial radius

The core idea of DeepONet is to construct the “basis” functions using the trunk network, while the branch network learns the corresponding “coefficients.” To enhance the performance of DeepONet, Lee *et al.* [56] proposed a novel two-step training strategy. In their approach, QR factorization is applied to the pretrained “basis” generated by the trunk network, followed by training the branch network. Building upon this framework, Peyvan *et al.* [14] further improved the method by employing singular value decomposition (SVD) as a replacement for QR decomposition. Following this idea, we applied the two-step training technique to BubbleONet. For more details on these applications, readers are referred to [56, 14].

The training process and network architecture are illustrated in Figure. 14. In the first step, a learnable variable A_m is introduced to mimic the latent representation from the branch network in single-step training. The trunk network is then trained to determine its optimal hyperparameters ϕ^* . Subsequently, the branch network is trained using the SVD-transformed output of the pretrained trunk network to find the optimal hyperparameters θ^* for the branch network. Both the trunk and branch networks share the same architecture: each consists of 8 layers with 512 neurons per layer. Rowdy activation function is applied to both branch net and trunk net with two sinusoidal

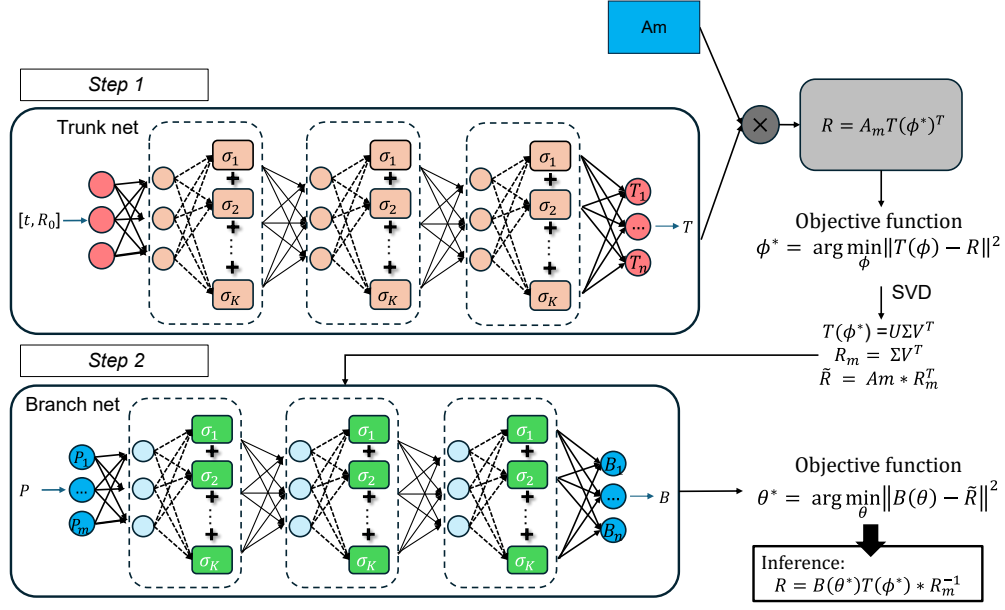


Figure 14: Two step training architecture for BubbleONet.

functions, initialized identically as in Eq. 7. The data, optimizer and other hyper parameters are the same as the case in section 5.2. The convergence history for both the trunk and branch networks is shown in Figure. 15. Meanwhile, a comparison of training time using different training technique shown in Table. 4. It can be observed that the two-step training is 20% faster compared to the single-step training process.

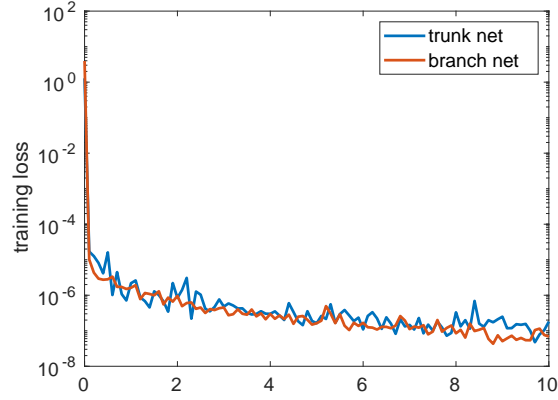


Figure 15: Convergence history of trunk net and branch net in two-step training.

Table 4: Comparison of training time for single-step and two-step training

Training	Time(h)
Single-step	72
Two-step	57.5

Validation results are presented in Figure. 16, which includes three representative cases. Cases (a) and (c) share the same parameters as Figure. 7(a) and Figure. 7(c), respectively: (a) corresponds

to a low-frequency case with a frequency of 523 kHz and an amplitude of 9×10^5 Pa, while (c) represents a high-frequency case with a frequency of 1927 kHz and an amplitude of 8×10^5 Pa. Both cases are well predicted, with mean square error of 4.93×10^{-3} and 2.79×10^{-4} , respectively. Figure. 16(b) corresponds to the same case as in Figure. 8, with a frequency of 900 kHz and a pressure amplitude of 9×10^5 Pa. The bubble profile is accurately predicted even without cross-validation.

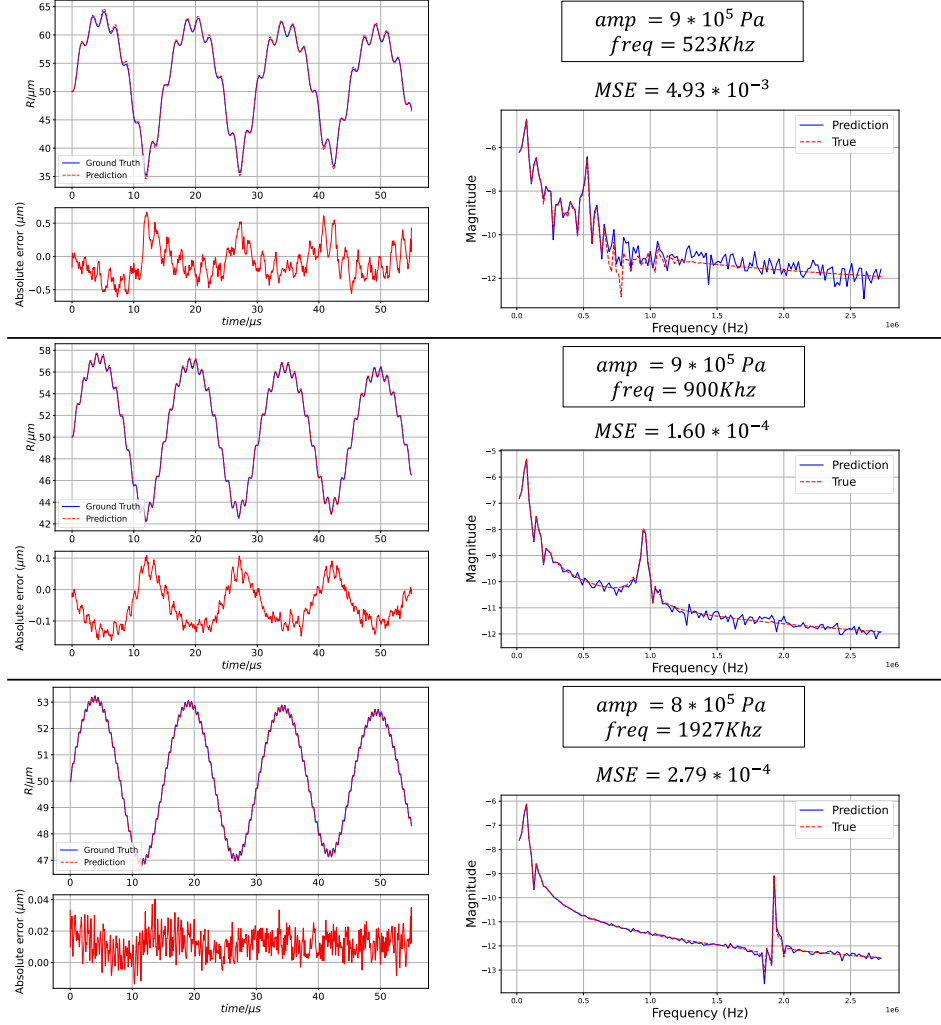


Figure 16: Validation of two-step training method for bubbles simulated using K-M equation with: (a) a frequency of 523 kHz and an amplitude of 9×10^5 Pa, (b) a frequency of 900 kHz and an amplitude of 9×10^5 Pa, and (c) a frequency of 1927 kHz and an amplitude of 8×10^5 Pa.

Interpolation is then conducted to evaluate the inference capability of the model. Figure. 17 shows four different frequencies: 600 kHz, 1000 kHz, 1300 kHz, and 2000 kHz for a pressure magnitude of 5.5×10^5 Pa. The corresponding MSEs are presented in Figure. 18. Similar periodical learning feature is observed but is different from the results in the previous section, where the number of sinusoidal functions is reduced in two-step training technique. Performance at lower frequencies, such as 600 kHz and 700 kHz, is worse compared to the single-step training, whereas performance at other frequencies improves, with reduced error, though still exhibiting periodic learning behavior. On the other hand, extrapolation to unseen frequencies results in higher errors

than single-step training, which may be attributed to the reduction of sinusoidal components in the rowdy activation function. An example of extrapolation at 2400 kHz, corresponding to the minimum MSE in that range, is shown in Figure. 19.

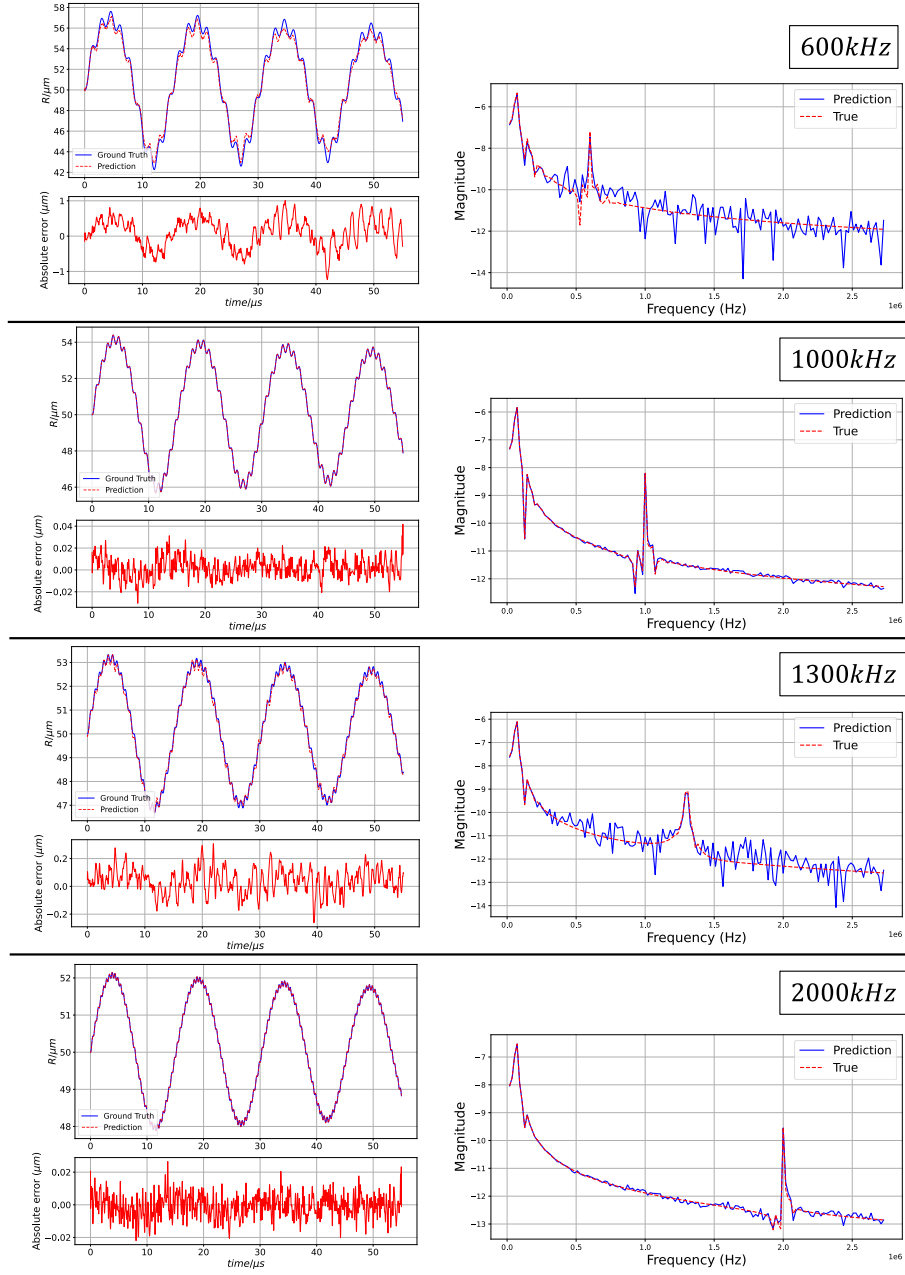


Figure 17: Time-domain and frequency-domain of interpolation results from two-step trained model for bubbles simulated at 600 kHz, 1000 kHz, 1300 kHz, and 2000 kHz, with a fixed amplitude of 5.5×10^5 Pa.

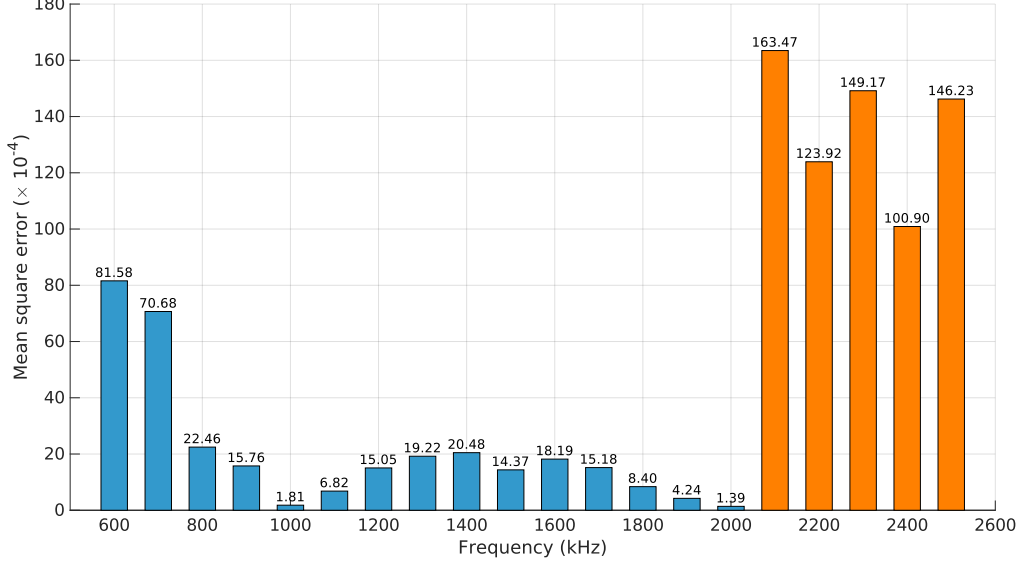


Figure 18: Mean square error across inference cases from two-step trained model with frequencies ranging from 600 kHz to 2500 kHz, at a fixed amplitude of 5.5×10^5 Pa. Blue bars represent the frequencies learned by the model, while orange bars indicate frequencies outside the training domain.

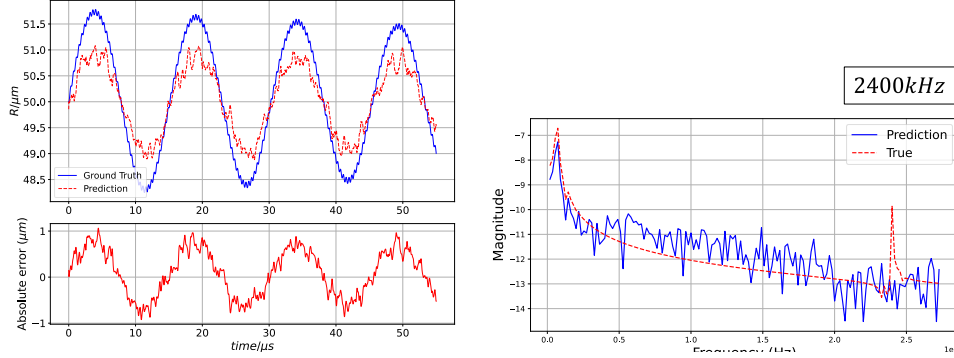


Figure 19: Time-domain and frequency-domain of extrapolation results of two-step trained model for bubbles driven at 2400 kHz, with a fixed amplitude of 5.5×10^5 Pa.

Another extrapolation on pressure amplitude is conducted under the same conditions as in Figure. 12, where the bubbles are simulated at 1000 kHz and 2000 kHz with a fixed amplitude of 11×10^5 Pa. The results are shown in Figure. 20. Compared to the single-step trained model, the MSEs are smaller— 4.41×10^{-3} and 3.96×10^{-4} , and the predictions closely match the ground truth.

The final set of extrapolation tests focuses on the bubble excitation time, in comparison with Fig. 13 as shown in Fig. 21. Using a pressure profile with an amplitude of 1×10^5 Pa and frequencies of 600 kHz and 2000 kHz, the simulation time is extended from $55 \mu\text{s}$ to $100 \mu\text{s}$. Although the two-step trained model performs better than the single-step model, it still fails to accurately predict the bubble dynamics at unseen time durations.

5.4. Two-step training for K-M equation with multi initial radii

In this section, we focus on the high-dimensional basis constructed by the trunk network, as illustrated in Figure. 22. Given n time sampling points and k different initial radii R_0 , meshgrids

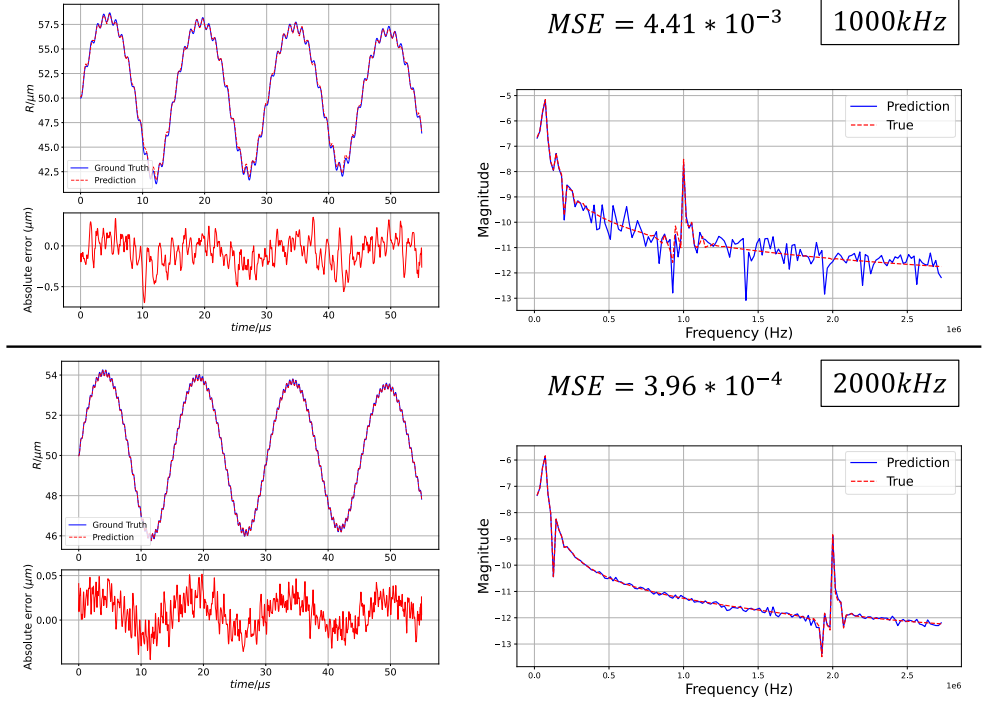


Figure 20: Time-domain and frequency-domain extrapolation results from two-step trained model for bubbles driven at 1000 kHz and 2000 kHz, with a fixed amplitude of 11×10^5 Pa.

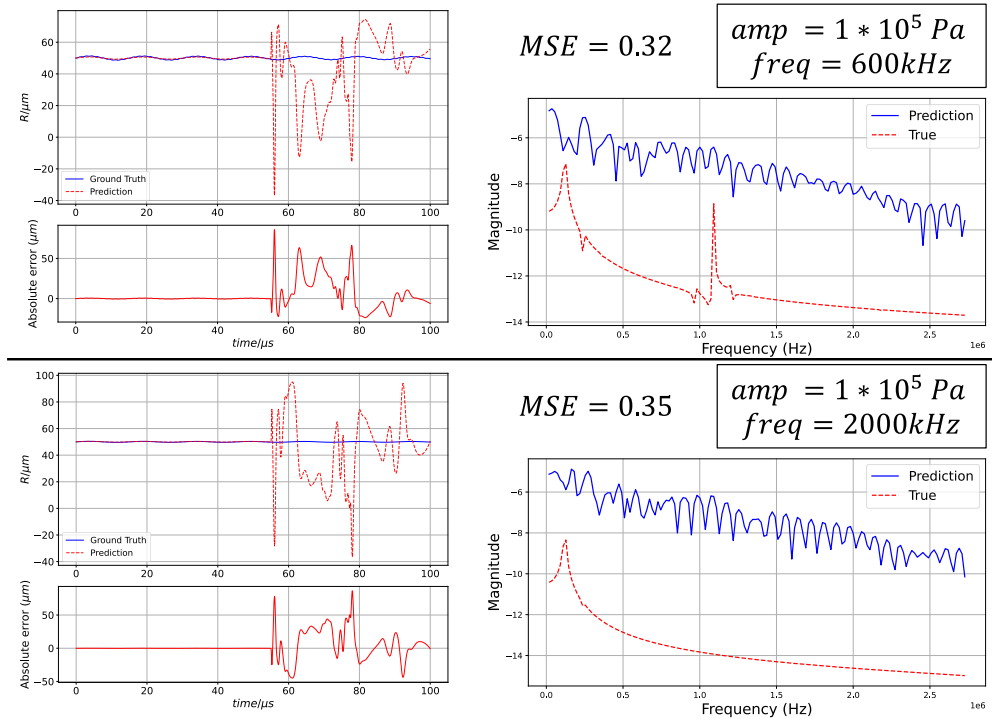


Figure 21: Time-domain and frequency-domain extrapolation results from two-step trained model for bubble dynamics over $100 \mu\text{s}$ driven at 600 kHz and 2000 kHz, with a fixed amplitude of 1×10^5 Pa.

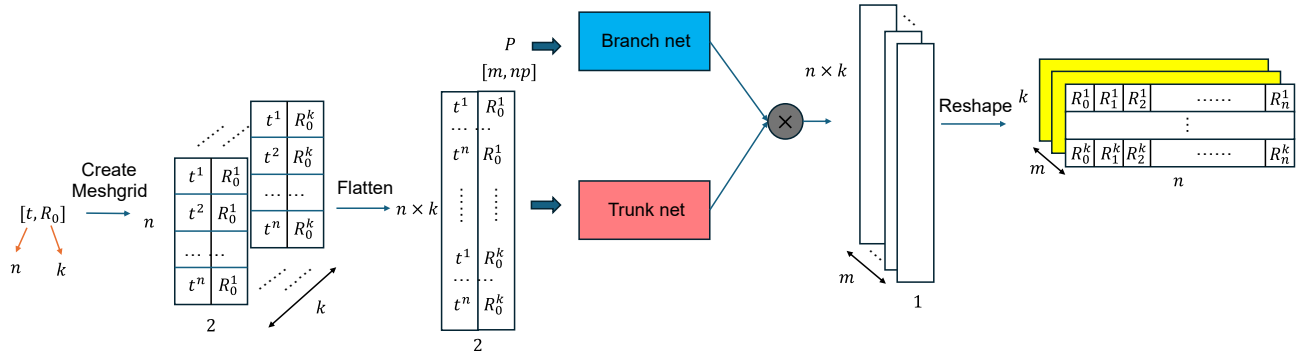


Figure 22: Implementation of multi-initial radii scenario, with initial radius and time as the input to trunk net.

of size $n \times k$ (time and radius) are generated for each R_0 , resulting in k meshgrids. These are flattened and stacked into a single input of size $(n \times k) \times 2$ for the trunk network. The branch network receives pressure profiles of size $m \times n_p$, where m is the batch size and n_p is the number of pressure sampling points. The model outputs predictions of size $m \times (n \times k)$, which are reshaped to $m \times k \times n$, representing bubble dynamics over time for each initial radius.

To showcase the capability, five initial radii, $50 \mu\text{m}$, $60 \mu\text{m}$, $70 \mu\text{m}$, $80 \mu\text{m}$ and $90 \mu\text{m}$, are considered. Pressure amplitudes and frequencies are sampled within the same ranges specified in Table 1, with 10 amplitude values and 30 frequency values, resulting in 300 distinct pressure profiles. For each initial radius, 300 bubble profiles are generated, totaling 1500 samples. Among these, 80% are used for training and 20% for validation. Consequently, the network architecture is adjusted to account for varying natural frequencies introduced by different initial radii. The Rowdy activation function incorporates four sinusoidal components to better capture these dynamics. The weight for loss function is then changed to $w_{\text{data}}=1, w_{\text{data}}=1000$, an additional term of initial radii is enforced as the initial condition(IC), with the weight $w_{\text{IC}} = 1$.

A prediction for bubbles subjected to a pressure oscillation with a frequency of 467 kHz and an amplitude of 9×10^5 Pa is presented in Figure. 23. In Figure. 23(a), the second peaks of all bubble profiles are highlighted with green circles and magnified on the right for clearer visualization. As shown in Figure. 23(b), all predicted profiles exhibit excellent agreement with the ground truth, with maximum absolute errors of approximately $0.2 \mu\text{m}$, corresponding to 0.40% for the $50 \mu\text{m}$ radius and 0.22% for the $90 \mu\text{m}$ radius.

A second prediction, shown in Figure. 24, considers bubbles subjected to a higher-frequency pressure oscillation of 1800 kHz with an amplitude of 3×10^5 Pa. As highlighted in Figure. 24(a), discrepancies in amplitude between the predicted and true profiles are observed at the second peaks (highlighted by green circles and magnified views). Nevertheless, the maximum absolute errors remain below $0.1 \mu\text{m}$, corresponding to 0.20% and 0.11% for the $50 \mu\text{m}$ and $90 \mu\text{m}$ radii, well within an acceptable range. Furthermore, FFT in Figure. 25 confirms that the model accurately captures both the natural and driving frequencies.

6. Conclusions

Bubble dynamics plays a critical role in many scientific and engineering domains, where rapid and accurate modeling is essential for understanding phase interactions and energy transfer in multiphase systems. While well-characterized by mathematical models such as the Rayleigh–Plesset and Keller–Miksis equations, the lack of efficient prediction methods for multi-bubble simulations limits its applicability in real-time and in-situ scenarios. In this paper, we propose a physics-informed neural

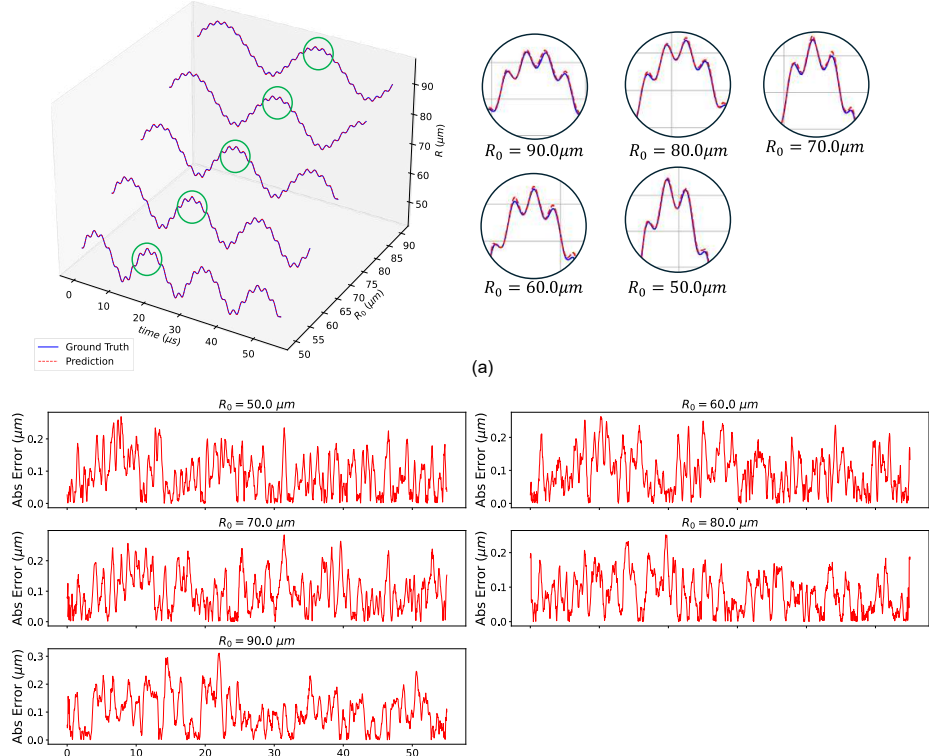


Figure 23: Prediction of bubble dynamics with five different initial radii, under pressure with a frequency of 467 kHz and an amplitude of 9×10^5 Pa. (a) Bubble profile with the second peak highlighted in green circles and shown on the right. (b) Absolute error.

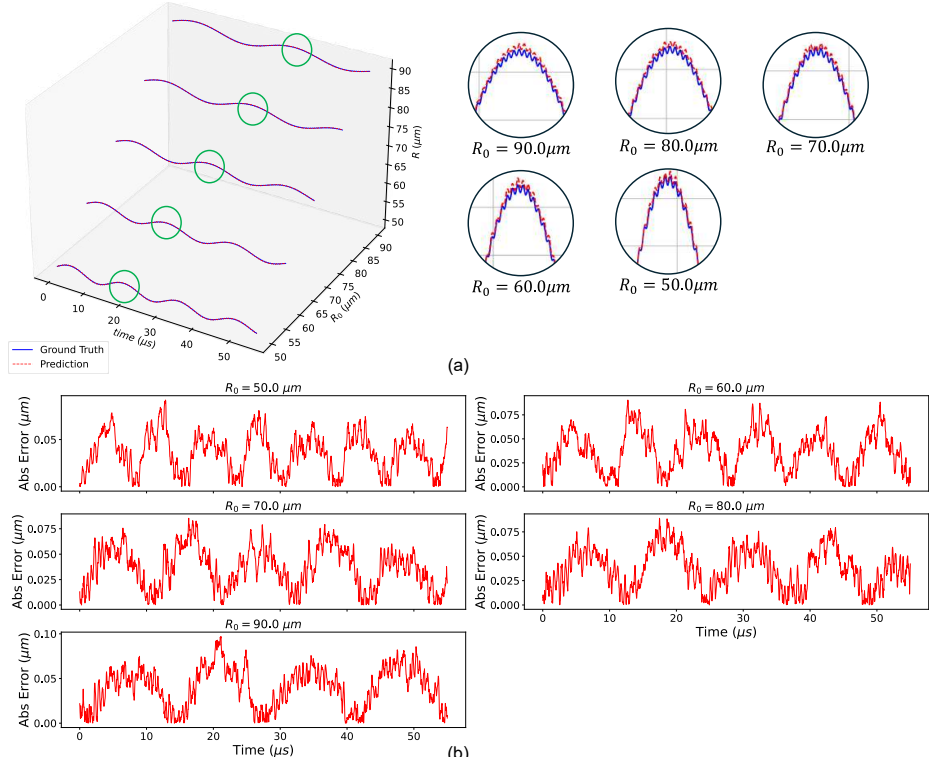


Figure 24: Prediction of bubble dynamics with five different initial radii, under pressure with a frequency of 1800 kHz and an amplitude of 3×10^5 Pa. (a) Bubble profile with the second peak highlighted in green circles and shown on the right. (b) Absolute error.

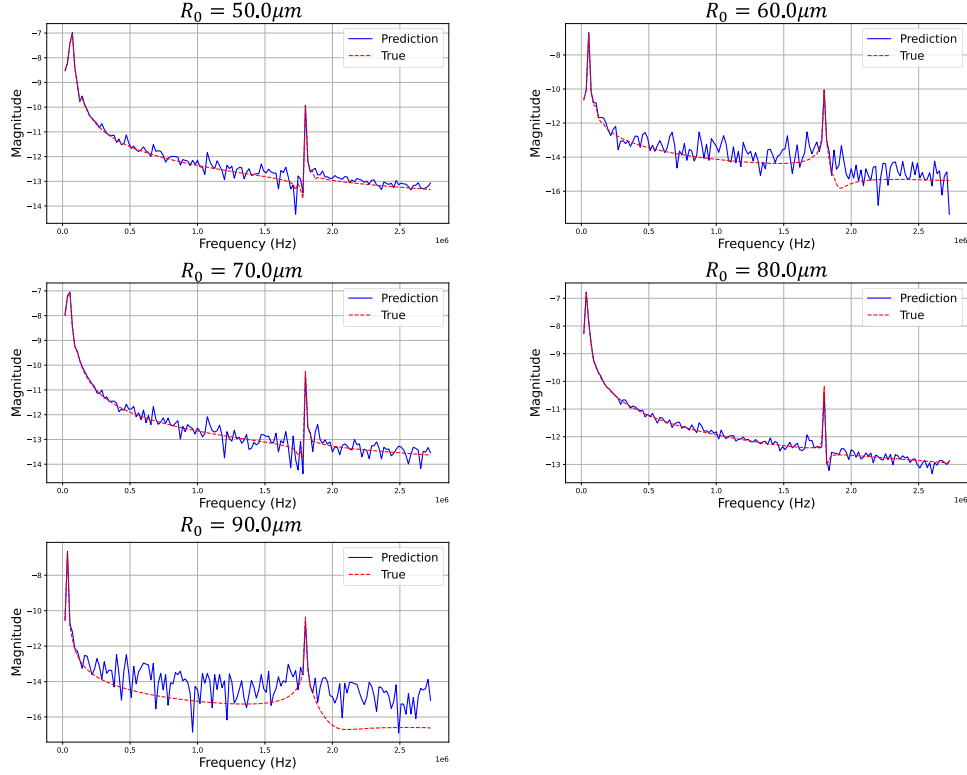


Figure 25: Fast Fourier Transform of predicted bubble dynamics with five different initial radii, under pressure with a frequency of 1800 kHz and an amplitude of 3×10^5 Pa.

operator model, BubbleONet, which leverages the function approximation capabilities of DeepONet to model macroscopic bubble dynamics. The framework accommodates bubbles governed by both the Rayleigh-Plesset equation and Keller-Miksis equation, and handles scenarios involving single and multiple initial radii. Key findings include:

1. The implementation of the Rowdy activation function effectively addresses spectral bias, enabling the model to accurately predict bubble dynamics across a wide range of pressure amplitudes and frequencies.
2. A comparison between single-step and two-step training techniques for BubbleONet demonstrates that the two-step approach significantly enhances the training process. It achieves faster convergence while maintaining comparable accuracy across validation, interpolation, and extrapolation scenarios.
3. The model is more sensitive to the frequency of the pressure than to its amplitude. Both training methods can capture natural and driving frequencies when extrapolating over amplitude; however, they struggle to predict accurately when extrapolating over frequency.

Despite its promising performance, the model exhibits several limitations that warrant further investigation. Notably, it currently fails to accurately capture bubble dynamics excited at its resonance frequency, which limits its current applicability in general turbulent flows, where a broad band spectrum of exciting frequencies, including the resonant frequency, is typically present. Further, its predictive capability remains constrained to the time domain represented in the training data, resulting in significant errors when evaluated on out-of-distribution samples. Ongoing research aims to address these challenges by improving the model's adaptability and generalization to unseen scenarios.

Appendix A. Non-dimensionalization of Rayleigh-Plesset Equation and Runge Kutta solution

Starting from the original R-P equation, written as:

$$R\ddot{R} + \frac{3}{2}\dot{R}^2 = \frac{1}{\rho} \left(P_B - P_\infty - 4\mu\frac{\dot{R}}{R} - \frac{2S}{R} \right), \quad (\text{A.1})$$

where the internal bubble pressure is given by

$$P_B = P_G = P_{G0} \left(\frac{R_0}{R} \right)^{3k}.$$

To nondimensionalize the R-P equation, we introduce the characteristic length $a = R_0$, time scale $\tau = t_{\max}$, and pressure scale P^* . The corresponding non-dimensional variables are defined as:

$$\bar{t} = \frac{t}{\tau}, \quad \bar{R} = \frac{R}{a}, \quad \bar{P} = \frac{P}{P^*}.$$

Differentiating the dimensional radius with respect to time yields:

$$\dot{R} = \frac{dR}{dt} = \frac{d(a\bar{R})}{d(\tau\bar{t})} = \frac{a}{\tau} \frac{d\bar{R}}{d\bar{t}} = \frac{a}{\tau} \dot{\bar{R}}, \quad (\text{A.2})$$

and similarly,

$$\ddot{R} = \frac{d^2R}{dt^2} = \frac{a}{\tau^2} \ddot{\bar{R}}. \quad (\text{A.3})$$

Substituting these expressions into Eq. (A.1) gives:

$$\frac{a^2}{\tau^2} \left(\bar{R}\ddot{\bar{R}} + \frac{3}{2}\dot{\bar{R}}^2 \right) = \frac{1}{\rho} \left(P_{G0} \left(\frac{1}{\bar{R}} \right)^{3k} - P^*\bar{P}_\infty - \frac{4\mu}{\tau} \frac{\dot{\bar{R}}}{\bar{R}} - \frac{2S}{a} \frac{1}{\bar{R}} \right). \quad (\text{A.4})$$

Dividing both sides by $\frac{a^2}{\tau^2}$, we obtain the nondimensional Rayleigh-Plesset equation:

$$\bar{R}\ddot{\bar{R}} + \frac{3}{2}\dot{\bar{R}}^2 = \frac{P_{G0}\tau^2}{\rho a^2} \left(\frac{1}{\bar{R}} \right)^{3k} - \frac{P^*\tau^2}{\rho a^2} \bar{P}_\infty - \frac{4\mu\tau}{\rho a^2} \frac{\dot{\bar{R}}}{\bar{R}} - \frac{2S\tau^2}{\rho a^3} \frac{1}{\bar{R}}. \quad (\text{A.5})$$

We define the pressure scale P^* as:

$$P^* = n \frac{\rho a^2}{\tau^2},$$

where n is a dimensionless scaling constant.

To simplify further, we introduce the Reynolds and Weber numbers as:

$$\begin{aligned} \text{Reynolds number: } Re &= \frac{\rho a^2}{\mu \tau}, \\ \text{Weber number: } We &= \frac{\rho a^3}{S \tau^2}. \end{aligned} \quad (\text{A.6})$$

Substituting these into the nondimensional equation, we obtain the final form:

$$\bar{R}\ddot{\bar{R}} + \frac{3}{2}\dot{\bar{R}}^2 = n\frac{P_{G0}}{P^*} \left(\frac{1}{\bar{R}}\right)^{3k} - n\bar{P}_\infty - \frac{4}{Re}\frac{\dot{\bar{R}}}{\bar{R}} - \frac{2}{We}\frac{1}{\bar{R}}. \quad (\text{A.7})$$

The Runge–Kutta solver for the non-dimensional R–P equation is written as:

$$\begin{aligned} \bar{y} &= \begin{bmatrix} \bar{R} \\ \dot{\bar{R}} \end{bmatrix}, \\ \dot{\bar{y}} &= \begin{bmatrix} \dot{\bar{R}} \\ \ddot{\bar{R}} \end{bmatrix} \\ &= \begin{bmatrix} \dot{\bar{R}} \\ \frac{1}{\bar{R}} \left(n\frac{P_{G0}}{P^*} \left(\frac{1}{\bar{R}}\right)^{3k} - n\bar{P}_\infty - \frac{4\mu\tau}{\rho a^2} \frac{\dot{\bar{R}}}{\bar{R}} - \frac{2S\tau^2}{\rho a^3} \frac{1}{\bar{R}} - \frac{3}{2}\dot{\bar{R}}^2 \right) \end{bmatrix}. \end{aligned} \quad (\text{A.8})$$

Appendix B. Non-dimensionalization of Keller-Miksis Equation and Runge Kutta solution

Starting from Eq. 3:

$$\left(1 - \frac{\dot{R}}{c}\right) R\ddot{R} + \frac{3}{2}\left(1 - \frac{\dot{R}}{3c}\right) \dot{R}^2 = \left(1 + \frac{\dot{R}}{c}\right) \frac{P_L - P_\infty}{\rho} + R \frac{\dot{P}_L - \dot{P}_\infty}{\rho c}, \quad (\text{B.1})$$

where the liquid pressure at the bubble wall is defined as

$$P_L = P_G - 4\mu \frac{\dot{R}}{R} - \frac{2S}{R},$$

and its time derivative is

$$\dot{P}_L = \dot{P}_G + 4\mu \left(\frac{\dot{R}^2}{R^2} - \frac{\ddot{R}}{R} \right),$$

with the gas pressure inside the bubble modeled as

$$P_G = P_{G0} \left(\frac{R_0}{R} \right)^{3k}.$$

To nondimensionalize the equation, we introduce characteristic scales:

$$a = R_0, \quad \tau = t_{\max}, \quad P^* = n \frac{\rho a^2}{\tau^2},$$

and define the nondimensional variables:

$$\bar{t} = \frac{t}{\tau}, \quad \bar{R} = \frac{R}{a}, \quad \bar{P} = \frac{P}{P^*}.$$

Differentiating the radius yields

$$\dot{R} = \frac{a}{\tau} \dot{\bar{R}}, \quad \ddot{R} = \frac{a}{\tau^2} \ddot{\bar{R}}.$$

Substituting these expressions into Eq. (B.1), we transform each term:

$$\left(1 - \frac{\dot{R}}{c}\right) R\ddot{R} = \frac{a^2}{\tau^2} \left(1 - \frac{a}{\tau c} \dot{R}\right) \bar{R}\ddot{\bar{R}}, \quad (\text{B.2})$$

$$\frac{3}{2} \left(1 - \frac{\dot{R}}{3c}\right) \dot{R}^2 = \frac{3}{2} \left(1 - \frac{a}{3\tau c} \dot{R}\right) \frac{a^2}{\tau^2} \dot{\bar{R}}^2, \quad (\text{B.3})$$

$$\left(1 + \frac{\dot{R}}{c}\right) \frac{P_L - P_\infty}{\rho} = \frac{1}{\rho} \left(1 + \frac{a}{\tau c} \dot{R}\right) \left(P_{G0} \bar{R}^{-3k} - \frac{2S}{a} \frac{1}{\bar{R}} - \frac{4\mu}{\tau} \frac{\dot{\bar{R}}}{\bar{R}} - P^* \bar{P}\right), \quad (\text{B.4})$$

$$R \frac{\dot{P}_L - \dot{P}_\infty}{\rho c} = \frac{a}{\rho c} \left[\frac{P_{G0}}{\tau} (-3k) \bar{R}^{-3k} \dot{\bar{R}} + \frac{2S}{\tau a} \frac{\dot{\bar{R}}}{\bar{R}} + \frac{4\mu}{\tau^2} \frac{\dot{\bar{R}}^2}{\bar{R}} - \frac{4\mu}{\tau^2} \ddot{\bar{R}} - \frac{P^*}{\tau} \bar{R} \dot{\bar{P}} \right]. \quad (\text{B.5})$$

Next, we define the following dimensionless number:

$$\begin{aligned} \text{Mach number: } M &= \frac{a}{\tau c}, \\ \text{Reynolds number: } Re &= \frac{\rho a^2}{\mu \tau}, \\ \text{Weber number: } We &= \frac{\rho a^3}{S \tau^2}. \end{aligned} \quad (\text{B.6})$$

Dividing the entire equation by $\frac{a^2}{\tau^2}$ yields the nondimensional form:

$$\begin{aligned} &\left(1 - M \dot{\bar{R}}\right) \bar{R}\ddot{\bar{R}} + \frac{3}{2} \left(1 - \frac{M}{3} \dot{\bar{R}}\right) \dot{\bar{R}}^2 \\ &= (1 + M \dot{\bar{R}}) \left[\frac{P_{G0} \tau^2}{\rho a^2} \left(\frac{1}{\bar{R}}\right)^{3k} - \frac{2}{We} \frac{1}{\bar{R}} - \frac{4}{Re} \frac{\dot{\bar{R}}}{\bar{R}} - \frac{P^* \tau^2}{\rho a^2} \bar{P} \right] \\ &+ M \left[\frac{P_{G0} \tau^2}{\rho a^2} (-3k) \left(\frac{1}{\bar{R}}\right)^{3k} \dot{\bar{R}} + \frac{2}{We} \frac{\dot{\bar{R}}}{\bar{R}} + \frac{4}{Re} \frac{\dot{\bar{R}}^2}{\bar{R}} - \frac{4}{Re} \ddot{\bar{R}} - \frac{P^* \tau^2}{\rho a^2} \bar{R} \dot{\bar{P}} \right]. \end{aligned} \quad (\text{B.7})$$

Finally, with n as a dimensionless scaling constant, we define

$$P^* = n \frac{\rho a^2}{\tau^2}$$

we obtain the fully nondimensionalized Keller–Miksis equation:

$$\begin{aligned} &\left(1 - M \dot{\bar{R}}\right) \bar{R}\ddot{\bar{R}} + \frac{3}{2} \left(1 - \frac{M}{3} \dot{\bar{R}}\right) \dot{\bar{R}}^2 \\ &= (1 + M \dot{\bar{R}}) \left[n \frac{P_{G0}}{P^*} \left(\frac{1}{\bar{R}}\right)^{3k} - \frac{2}{We} \frac{1}{\bar{R}} - \frac{4}{Re} \frac{\dot{\bar{R}}}{\bar{R}} - n \bar{P} \right] \\ &+ M \left[n \frac{P_{G0}}{P^*} (-3k) \left(\frac{1}{\bar{R}}\right)^{3k} \dot{\bar{R}} + \frac{2}{We} \frac{\dot{\bar{R}}}{\bar{R}} + \frac{4}{Re} \frac{\dot{\bar{R}}^2}{\bar{R}} - \frac{4}{Re} \ddot{\bar{R}} - n \bar{R} \dot{\bar{P}} \right]. \end{aligned} \quad (\text{B.8})$$

The resulting system for a Runge–Kutta (RK) solver is expressed in first-order form as:

$$\bar{y} = \begin{bmatrix} \bar{R} \\ \dot{\bar{R}} \end{bmatrix},$$

$$\dot{\bar{y}} = \begin{bmatrix} \dot{\bar{R}} \\ \frac{1}{\left(1 - M\dot{\bar{R}}\right) \bar{R} + \frac{4M}{Re}} \left((1 + M\dot{\bar{R}}) \left[n \frac{P_{G0}}{P^*} \left(\frac{1}{\bar{R}} \right)^{3k} - \frac{2}{We} \frac{1}{\bar{R}} - \frac{4}{Re} \frac{\dot{\bar{R}}}{\bar{R}} - n\bar{P} \right] \right. \\ \left. + M \left[-3k n \frac{P_{G0}}{P^*} \left(\frac{1}{\bar{R}} \right)^{3k} \dot{\bar{R}} + \frac{2}{We} \frac{\dot{\bar{R}}}{\bar{R}} + \frac{4}{Re} \frac{\dot{\bar{R}}^2}{\bar{R}} - n\bar{R}\dot{\bar{P}} \right] \right. \\ \left. - \frac{3}{2} \left(1 - \frac{M}{3} \dot{\bar{R}} \right) \dot{\bar{R}}^2 \right) \end{bmatrix}. \quad (\text{B.9})$$

References

- [1] E. C. Pua, P. Zhong, Ultrasound-mediated drug delivery, *IEEE engineering in medicine and biology magazine* 28 (1) (2009) 64–75.
- [2] A. Gnanaskandan, C.-T. Hsiao, G. Chahine, Modeling of microbubble-enhanced high-intensity focused ultrasound, *Ultrasound in medicine & biology* 45 (7) (2019) 1743–1761.
- [3] E. Cako, Z. Wang, R. Castro-Muñoz, M. P. Rayaroth, G. Boczkaj, Cavitation based cleaner technologies for biodiesel production and processing of hydrocarbon streams: A perspective on key fundamentals, missing process data and economic feasibility—a review, *Ultrasonics sonochemistry* 88 (2022) 106081.
- [4] A. Gnanaskandan, K. Mahesh, Large eddy simulation of the transition from sheet to cloud cavitation over a wedge, *International Journal of Multiphase Flow* 83 (2016) 86–102.
- [5] L. Rayleigh, Viii. on the pressure developed in a liquid during the collapse of a spherical cavity, *The London, Edinburgh, and Dublin Philosophical Magazine and Journal of Science* 34 (200) (1917) 94–98.
- [6] J.-P. Franc, The rayleigh-plesset equation: a simple and powerful tool to understand various aspects of cavitation, in: *Fluid dynamics of cavitation and cavitating turbopumps*, Springer, 2007, pp. 1–41.
- [7] C. E. Brennen, *Cavitation and bubble dynamics*, Cambridge university press, 2014.
- [8] J. B. Keller, M. Miksis, Bubble oscillations of large amplitude, *The Journal of the Acoustical Society of America* 68 (2) (1980) 628–633.
- [9] A. Prosperetti, A. Lezzi, Bubble dynamics in a compressible liquid. part 1. first-order theory, *Journal of Fluid Mechanics* 168 (1986) 457–478.
- [10] F. R. Gilmore, The growth or collapse of a spherical bubble in a viscous compressible liquid, Vol. 26, *California Institute of Technology Pasadena, CA*, 1952.
- [11] L. Lu, P. Jin, G. Pang, Z. Zhang, G. E. Karniadakis, Learning nonlinear operators via DeepONet based on the universal approximation theorem of operators, *Nature Machine Intelligence* 3 (3) (2021) 218–229. doi:10.1038/s42256-021-00302-5.
- [12] Z. Mao, L. Lu, O. Marxen, T. A. Zaki, G. E. Karniadakis, DeepM&Mnet for hypersonics: Predicting the coupled flow and finite-rate chemistry behind a normal shock using neural-network approximation of operators, *Journal of Computational Physics* 447 (2021) 1–24. arXiv:2011.03349, doi:10.1016/j.jcp.2021.110698.
- [13] P. Jin, S. Meng, L. Lu, MIONet: Learning multiple-input operators via tensor product, *SIAM Journal on Scientific Computing* 44 (6) (2022) A3490–A3514.
- [14] A. Peyvan, V. Oommen, A. D. Jagtap, G. E. Karniadakis, RiemannONets: Interpretable neural operators for Riemann problems, *Computer Methods in Applied Mechanics and Engineering* 426 (April) (2024) 116996. arXiv:2401.08886, doi:10.1016/j.cma.2024.116996. URL <https://doi.org/10.1016/j.cma.2024.116996>

- [15] S. Goswami, A. D. Jagtap, H. Babae, B. T. Susi, G. E. Karniadakis, Learning stiff chemical kinetics using extended deep neural operators, *Computer Methods in Applied Mechanics and Engineering* 419 (2024) 116674.
- [16] J. D. Osorio, Z. Wang, G. Karniadakis, S. Cai, C. Chrysostomidis, M. Panwar, R. Hovsapien, Forecasting solar-thermal systems performance under transient operation using a data-driven machine learning approach based on the deep operator network architecture, *Energy Conversion and Management* 252 (2022) 115063.
- [17] M. Raissi, P. Perdikaris, G. E. Karniadakis, Physics-informed neural networks: A deep learning framework for solving forward and inverse problems involving nonlinear partial differential equations, *Journal of Computational Physics* 378 (2019) 686–707. doi:10.1016/j.jcp.2018.10.045. URL <https://doi.org/10.1016/j.jcp.2018.10.045>
- [18] G. E. Karniadakis, I. G. Kevrekidis, L. Lu, P. Perdikaris, S. Wang, L. Yang, Physics-informed machine learning, *Nature Reviews Physics* 3 (6) (2021) 422–440. doi:10.1038/s42254-021-00314-5.
- [19] A. D. Jagtap, E. Kharazmi, G. E. Karniadakis, Conservative physics-informed neural networks on discrete domains for conservation laws: Applications to forward and inverse problems, *Computer Methods in Applied Mechanics and Engineering* 365 (2020) 113028.
- [20] A. D. Jagtap, G. E. Karniadakis, Extended physics-informed neural networks (xpinns): A generalized space-time domain decomposition based deep learning framework for nonlinear partial differential equations, *Communications in Computational Physics* 28 (5) (2020).
- [21] M. Penwarden, A. D. Jagtap, S. Zhe, G. E. Karniadakis, R. M. Kirby, A unified scalable framework for causal sweeping strategies for physics-informed neural networks (pinns) and their temporal decompositions, *Journal of Computational Physics* 493 (2023) 112464.
- [22] Z. Hu, A. D. Jagtap, G. E. Karniadakis, K. Kawaguchi, Augmented physics-informed neural networks (apinns): A gating network-based soft domain decomposition methodology, *Engineering Applications of Artificial Intelligence* 126 (2023) 107183.
- [23] K. Shukla, A. D. Jagtap, J. L. Blackshire, D. Sparkman, G. E. Karniadakis, A physics-informed neural network for quantifying the microstructural properties of polycrystalline nickel using ultrasound data: A promising approach for solving inverse problems, *IEEE Signal Processing Magazine* 39 (1) (2021) 68–77.
- [24] A. D. Jagtap, D. Mitsotakis, G. E. Karniadakis, Deep learning of inverse water waves problems using multi-fidelity data: Application to serre–green–naghdi equations, *Ocean Engineering* 248 (2022) 110775.
- [25] J. Abbasi, B. Moseley, T. Kurotori, A. D. Jagtap, A. R. Kavscek, A. Hiorth, P. Ø. Andersen, History-matching of imbibition flow in fractured porous media using physics-informed neural networks (pinns), *Computer Methods in Applied Mechanics and Engineering* 437 (2025) 117784.
- [26] J. Abbasi, A. D. Jagtap, B. Moseley, A. Hiorth, P. Ø. Andersen, Challenges and advancements in modeling shock fronts with physics-informed neural networks: A review and benchmarking study, *arXiv preprint arXiv:2503.17379* (2025).

- [27] Q. Zhu, Z. Liu, J. Yan, Machine learning for metal additive manufacturing: predicting temperature and melt pool fluid dynamics using physics-informed neural networks, *Computational Mechanics* 67 (2) (2021) 619–635. arXiv:2008.13547, doi:10.1007/s00466-020-01952-9.
- [28] Z. Mao, A. D. Jagtap, G. E. Karniadakis, Physics-informed neural networks for high-speed flows, *Computer Methods in Applied Mechanics and Engineering* 360 (2020) 112789. doi:10.1016/j.cma.2019.112789.
URL <https://doi.org/10.1016/j.cma.2019.112789>
- [29] A. D. Jagtap, Z. Mao, N. Adams, G. E. Karniadakis, Physics-informed neural networks for inverse problems in supersonic flows, *Journal of Computational Physics* 466 (2022) 111402.
- [30] L. Cheng, G. J. Wagner, A representative volume element network (RVE-net) for accelerating RVE analysis, microscale material identification, and defect characterization, *Computer Methods in Applied Mechanics and Engineering* 390 (feb 2022). doi:10.1016/j.cma.2021.114507.
- [31] Y. Zhu, N. Zabaras, P. S. Koutsourelakis, P. Perdikaris, Physics-constrained deep learning for high-dimensional surrogate modeling and uncertainty quantification without labeled data, *Journal of Computational Physics* 394 (2019) 56–81. arXiv:1901.06314, doi:10.1016/j.jcp.2019.05.024.
URL <https://doi.org/10.1016/j.jcp.2019.05.024>
- [32] Z. Hu, K. Shukla, G. E. Karniadakis, K. Kawaguchi, Tackling the curse of dimensionality with physics-informed neural networks, *Neural Networks* 176 (2024) 106369.
- [33] S. S. Menon, A. D. Jagtap, Anant-net: Breaking the curse of dimensionality with scalable and interpretable neural surrogate for high-dimensional pdes, arXiv preprint arXiv:2505.03595 (2025).
- [34] T. De Ryck, A. D. Jagtap, S. Mishra, Error estimates for physics-informed neural networks approximating the navier–stokes equations, *IMA Journal of Numerical Analysis* 44 (1) (2024) 83–119.
- [35] Z. Hu, A. D. Jagtap, G. E. Karniadakis, K. Kawaguchi, When do extended physics-informed neural networks (xpinns) improve generalization?, arXiv preprint arXiv:2109.09444 (2021).
- [36] Y. Shin, J. Darbon, G. E. Karniadakis, On the convergence of physics informed neural networks for linear second-order elliptic and parabolic type pdes, arXiv preprint arXiv:2004.01806 (2020).
- [37] H. N. Mhaskar, E. Tsoukanis, A. D. Jagtap, An approximation theory perspective on machine learning, arXiv preprint arXiv:2506.02168 (2025).
- [38] C. Lin, M. Maxey, Z. Li, G. E. Karniadakis, A seamless multiscale operator neural network for inferring bubble dynamics, *Journal of Fluid Mechanics* 929 (2021) 1–14. doi:10.1017/jfm.2021.866.
- [39] C. Lin, Z. Li, L. Lu, S. Cai, M. Maxey, G. E. Karniadakis, Operator learning for predicting multiscale bubble growth dynamics, *Journal of Chemical Physics* 154 (10) (2021). arXiv:2012.12816, doi:10.1063/5.0041203.
- [40] S. Wang, H. Wang, P. Perdikaris, Learning the solution operator of parametric partial differential equations with physics-informed DeepONets, *Science Advances* 7 (40) (2021) 1–9. arXiv:2103.10974, doi:10.1126/sciadv.abi8605.

- [41] S. Goswami, M. Yin, Y. Yu, G. E. Karniadakis, A physics-informed variational DeepONet for predicting crack path in quasi-brittle materials, *Computer Methods in Applied Mechanics and Engineering* 391 (2022) 114587. doi:10.1016/j.cma.2022.114587.
URL <https://doi.org/10.1016/j.cma.2022.114587>
- [42] L. Lu, X. Meng, Z. Mao, G. E. Karniadakis, DeepXDE: A deep learning library for solving differential equations, *SIAM Review* 63 (1) (2021) 208–228. doi:10.1137/19M1274067.
- [43] F. Denner, S. Schenke, Apecss: A software library for cavitation bubble dynamics and acoustic emissions, *Journal of Open Source Software* 8 (86) (2023) 5435. doi:10.21105/joss.05435.
URL <https://doi.org/10.21105/joss.05435>
- [44] Y. Zhang, L. Cheng, A. Gnanaskandan, Physics informed operator learning for predicting bubble dynamics, in: *Fluids Engineering Division Summer Meeting, American Society of Mechanical Engineers*, 2025.
- [45] Y. Hong, M. Li, X. He, J. T. Xing, Energy flow investigations of Rayleigh-Plesset equation for cavitation simulations, *Ocean Engineering* 306 (April) (2024) 118072. doi:10.1016/j.oceaneng.2024.118072.
URL <https://doi.org/10.1016/j.oceaneng.2024.118072>
- [46] A. D. Jagtap, Y. Shin, K. Kawaguchi, G. E. Karniadakis, Deep Kronecker neural networks: A general framework for neural networks with adaptive activation functions, *Neurocomputing* 468 (2022) 165–180. arXiv:2105.09513, doi:10.1016/j.neucom.2021.10.036.
URL <https://doi.org/10.1016/j.neucom.2021.10.036>
- [47] Y. Cao, Z. Fang, Y. Wu, D. X. Zhou, Q. Gu, Towards Understanding the Spectral Bias of Deep Learning, *IJCAI International Joint Conference on Artificial Intelligence* (2021) 2205–2211 arXiv:1912.01198, doi:10.24963/ijcai.2021/304.
- [48] N. Rahaman, A. Baratin, D. Arpit, F. Draxler, M. Lin, F. A. Hamprecht, Y. Bengio, A. Courville, On the spectral bias of neural networks, *36th International Conference on Machine Learning, ICML 2019 2019-June* (1) (2019) 9230–9239. arXiv:1806.08734.
- [49] C. Gulcehre, M. Moczulski, M. Denil, Y. Bengio, Noisy activation functions, *33rd International Conference on Machine Learning, ICML 2016 6* (2016) 4457–4466. arXiv:1603.00391.
- [50] K. Shridhar, J. Lee, H. Hayashi, P. Mehta, B. K. Iwana, S. Kang, S. Uchida, S. Ahmed, A. Dengel, ProbAct: A Probabilistic Activation Function for Deep Neural Networks, *arXiv preprint arXiv:1905.10761* (2019). arXiv:1905.10761.
URL <http://arxiv.org/abs/1905.10761>
- [51] F. Agostinelli, M. Hoffman, P. Sadowski, P. Baldi, Learning activation functions to improve deep neural networks, *arXiv preprint arXiv:1412.6830* (2014).
- [52] A. D. Jagtap, K. Kawaguchi, G. E. Karniadakis, Adaptive activation functions accelerate convergence in deep and physics-informed neural networks, *Journal of Computational Physics* 404 (2020) 109136. arXiv:1906.01170, doi:10.1016/j.jcp.2019.109136.
URL <https://doi.org/10.1016/j.jcp.2019.109136>

- [53] A. D. Jagtap, K. Kawaguchi, G. Em Karniadakis, Locally adaptive activation functions with slope recovery for deep and physics-informed neural networks, *Proceedings of the Royal Society A* 476 (2239) (2020) 20200334.
- [54] A. D. Jagtap, G. E. Karniadakis, How important are activation functions in regression and classification? a survey, performance comparison, and future directions, *Journal of Machine Learning for Modeling and Computing* 4 (1) (2023).
- [55] J. R. Dormand, P. J. Prince, A family of embedded Runge-Kutta formulae, *Journal of Computational and Applied Mathematics* 15 (2) (1986) 203–211. doi:10.1016/0377-0427(86)90027-0.
- [56] S. Lee, Y. Shin, on the Training and Generalization of Deep Operator Networks, *SIAM Journal on Scientific Computing* 46 (4) (2024) C273–C296. arXiv:2309.01020, doi:10.1137/23M1598751.